PARTIAL OXIDATION OF HYDROCARBONS OVER CERIA ZIRCONIA CATALYSTS

A Thesis
Presented to
The Academic Faculty

by

Olivia Camille Williams

In Partial Fulfillment
of the Requirements for the Degree
Masters of Science in the
School of Chemical and Biomolecular Engineering

Georgia Institute of Technology
[May 2022]

PARTIAL OXIDATION OF HYDROCARBONS OVER CERIA ZIRCONIA CATALYSTS

Approved by:

Dr. Carsten Sievers, Advisor
School of Chemical and Biomolecular Engineering
Georgia Institute of Technology

Dr. Ryan P. Lively
School of Chemical and Biomolecular Engineering
Georgia Institute of Technology

Dr. Andrew J. Medford
School of Chemical and Biomolecular Engineering
Georgia Institute of Technology

Date Approved: [January 28, 2022]

ACKNOWLEDGEMENTS

I would like to thank my parents and brother for their continued support. I would like to thank my lab-mates, too, for their assistance and friendship, as well as Dr. Sievers. The beautiful STEM images were captured by Yong Ding and I profusely thank him. Pearl Kwon at Micromeritics performed the TPR analysis on my catalysts and I greatly appreciated her assistance. Also, I am grateful for the help from Nhu "Ty" Nguyen with the high temperature TGA tests. This research was funded by the U.S. Department of Energy, Office of Basic Energy Sciences, Chemical Sciences, Geosciences, and Biosciences Division under Award Number DE-SC0016486.

TABLE OF CONTENTS

LIST OF TABLES

LIST OF FIGURES

LIST OF SYMBOLS AND ABBREVIATIONS

CZ	Ceria Zirconia
MES	Modulation Excitation Spectroscopy
MMO	Methane Monooxygenase

SUMMARY

This thesis describes research along several avenues pertaining to oxidation reactions. First, the major conclusions are summarized from a perspective describing active oxygen species on catalyst surfaces. Some oxygen species are more selective than others and if these species were better understood, a catalyst surface could be tuned to produce those selective species instead of unselective ones. However, these species readily interconvert and there does not exist a single analytical method which can characterize—and differentiate—between all of the possible species. Due to this situation, analytical techniques are focused upon in that paper. The most promising analytical technique is isotope exchange coupled with infrared spectroscopy and an inline mass spectrometer.

Next, methane partial oxidation over ceria zirconia catalysts is studied with infrared spectroscopy. Methane and oxygen concentrations are modulated to differentiate active and spectator species via modulation excitation spectroscopy. Aromatic and alkoxy surface species modulate in sync with each other, supporting the hypothesis that these species compete with each other in the partial oxidation of methane to methanol; formates are formed in all cases, and these species are associated with the complete combustion of methane to carbon dioxide and water. Chemical looping may be an appropriate reaction engineering method to increase the yield of selective oxidation products since the formate and alkoxy species were separated during the oxygen modulation experiment over nickel-copper on ceria zirconia.

Finally, two reactions (water splitting and heptane partial oxidation) catalyzed under mechanical forces are explored. It was hypothesized that oxygen could be

mechanically driven from the ceria lattice. Oxygen from water would then replenish the lattice, releasing hydrogen. Due to iron contamination from the steel vessel, this hypothesis cannot be confirmed. Ceria zirconia, when milled in the presence of heptane, exhibits infrared bands in the C-O stretching region, leading to the conclusion that some sort of oxidative reaction occurs during milling. Additional study needs be performed to describe this system fully.

CHAPTER 1. INTRODUCTION

Selective oxidation allows for the production of a vast quantity of intermediates and monomers such as formaldehyde from methanol, acrylic acid from propylene, and the production of maleic anhydride from n-butane [1,2]. Many parties, due to the ubiquitous nature of oxidative processes, have funded research to probe many aspects of these reactions; after all, catalytic processes which produce chemicals account for nearly 25% of industrial energy use [3]. Yet many processes still offer opportunities for refinements—especially as relates to sustainability[1,2]—and many questions remain unanswered.

One issue of sustainability which many have attempted to address is the human handling of methane. Certainly, leaks and intermittent sources crop up; however, over nearly 400,000 million ft^3 of natural gas was vented or flared in the United States in 2020 [4]. Methane is a far more potent greenhouse gas than carbon dioxide [5], but these emissions, either as methane or carbon dioxide, provide no useful energy. Due to this situation, many researchers have studied various methods of methane valorization. Waste reduction, in terms of energy and molecular elegance, during methanol synthesis has been a favorite topic of study [6]. It seems that selectivity of methane to methanol in direct/continuous processes is nearly catalyst independent [7], and so reaction engineering approaches seem to be a more promising direction than additional catalyst screenings. Reaction engineering approaches are probed in this thesis.

Another sustainability issue associated with methane is hydrogen production. Most hydrogen in the United States is produced from steam methane reforming [8]. Water, as a non-hydrocarbon feed source, may also be split to form hydrogen and oxygen. This process

requires tremendous energy input. Researchers have managed to split water in a traditional thermal reaction, with the substantial thermal energy supplied by concentrated solar energy [9–11]. A more novel method some have used is mechanochemistry [12–17]. The method of mechanochemistry will be entertained in this thesis.

CHAPTER 2. ACTIVE OXYGEN SPECIES IN HETEROGENEOUS CATALYZED OXIDATION REACTIONS

The active oxygen species that participate in selective oxidation reactions have not been adequately characterized at reasonable reaction temperatures and pressures [18]. The ground state of molecular oxygen is a triplet diradical ground state, with two unpaired electrons in different antibonding orbitals [19]. Hydrocarbons in the ground state are in a singlet state with a closed shell electronic structure; chemical reactions between singlet and triplet states to yield single state products are forbidden (it is possible for a 'forbidden' reaction to occur via spin-inversion, effected by a heavy metal with unpaired electrons close in energy to the ground state) [6,19,20].

The most commonly exploited way to overcome the spin state problem is to activate oxygen by a transition metal in a specific oxidation state [20]. An appropriate oxidation state is one where the metal center becomes paramagnetic and contains unpaired electrons; the metal center donates on electron to generate superoxide and form a neutral metal-oxide complex [20] (Figure 2. 1).

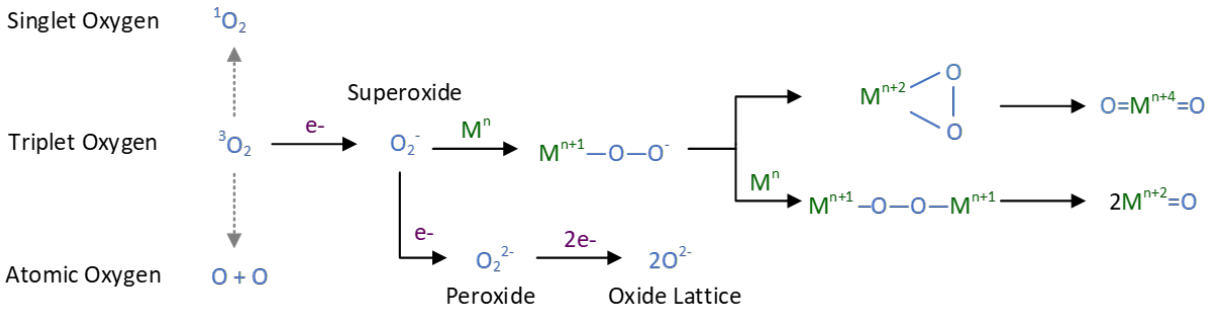

Figure 2. 1 Formation of various active oxygen species with metal centers (M) on metal oxide surfaces. It should be noted that all of the intermediate species should be considered active. Adapted from multiple figures published in [6]

Ideal oxygen activation routes like those shown in Figure 2. 1 do not involve free-radical species [20]. Free radical species tend to initiate unselective oxidation (it should be noted that peroxide will thermally decompose above 130-150°C and some transition metals like Mn, Fe, Co, Ni, and Cu can induce peroxide cleavage) [20]. Biological systems will produce free-radicals, but in a controlled process where scavengers keep concentrations low; deregulation of radical oxygen formation causes stress and destruction in these systems [19,21].

Several types of active oxygen have been found on various surface types: several configurations of lattice oxygen as well as surface species like superoxide (O_2^-), O^-, peroxide (O_2^{2-}), and hydroxyl groups. These species are not all active at the same conditions (surface type, temperature, pressure, etc.) and may lead to different reaction pathways. They also rapidly interconvert. There is no universal technique to characterize every possible active oxygen species, and so conclusions are often not unique [6,18,22]. If active oxygen species could be thoroughly understood, then catalytic surfaces could be

tailored to produce more selective species, which would improve yield and selectivity for selective oxygen reactions.

A perspective was composed to discuss the current scientific understanding of the subject [18]. Biologic systems as well as inorganic systems, including zeolites, reducible metal oxides, and supported noble metals, are overviewed. There is little agreement as to which is the most selective or active species, but it seems that electron localization over a single atom is necessary to activate very stable C—H bonds like those in methane. As was noted before, the fact that there is no analytical method that can characterize all the possible active oxygen species impedes study in this area. Since this is a major limiting factor, analytical methods were emphasized in this publication. Florescence and other color-changing assays may be used, but these methods are often constrained by temperature, pH, and reaction phase. Infrared, Raman, and Ultra-Violet spectroscopies have been used, but short-lived species are not recorded. Electron Paramagnetic Resonance spectroscopy can record short lived species, but only those that are paramagnetic (O_2^-, O^-, O_3^-) are visible. X-ray Photoelectron Spectroscopy may be used but these tests are not conducted at realistic temperature and pressure; Resonant Inelastic soft X-ray Scattering Spectroscopy may also provide useful information, but this technique requires a synchrotron and a homogenous material—and many catalysts are not homogeneous. Oxygen temperature programed desorption and oxygen storage capacity will give information about the quantity of oxygen species but will not differentiate between types of species. The most promising experimental approach is oxygen isotope exchange coupled with infrared and mass spectrometry, but computational methods allow for many additional fundamental insights. A more in-depth discussion may be found in reference [18].

CHAPTER 3. STUDY OF METHANE PARTIAL OXIDATION TO METHANOL WITH MODULATION EXCITATION SPECTROSCOPY

3.1 Introduction

The partial oxidation of methane to methanol has been studied for decades over inorganic catalysts [6,23]. The United States alone had proven natural gas reserves of nearly 500 trillion cubic feet in 2019 [24]. These reserves, however, are located far from population centers and methane is often flared because there is no economically viable method to transport it [25]. If this gas could be cheaply converted into an easily pumped fluid, for example methanol, these resources could be transported to refining centers and more effectively consumed.

Methane is a remarkably stable molecule, symmetric with a bond energy of 440 kJ/mol [25]. Methanol therefore is commonly produced from synthetic gas (syngas), products of the combustion of methane over nickel deposited on refractory alumina or similar ceramic material [26]. Methanol production from syngas proceeds over alumina supported copper and zinc oxides at 200-300°C and 50-100 bar [26]. This multiple step reaction cycle at elevated pressure requires large capital inputs, which makes its implementation at distributed well-sites impractical [6]. A direct synthesis method, therefore, is desirable. Methane monooxygenases (MMO) are metalloenzymes capable of the direct synthesis of methanol from methane. Two types of MMOs are sometimes expressed, one with an iron active site, one with a copper active site [27,28]. Iron and

copper on zeolites are capable of transforming methane to methanol and similarities have been noted between these systems and the biological counterparts [29–34].

Establishing structure-activity relationships at functioning catalytic conditions can improve catalytic system design [3]. It has been shown that bimetallic catalysts exhibit properties distinct from—and usually more advantageous than—their monometallic counterparts [8,35–37]. Particle size is often affected—as is acidity, charge, and geometric structure. Doped ceria zirconia catalysts will produce methanol at steady state [38–41]. Surface moieties, including methyl, carbonate, formate, aromatic ring, and alkoxy vibrational modes, produced on nickel doped ceria zirconia during methane partial oxidation have been observed [42]; however, spectator groups were not differentiated from active intermediates and bimetallic doped ceria zirconia was also not analyzed.

Modulation Excitation Spectroscopy (MES) allows one to differentiate between active and spectator species [43–48]. An external stimulus is modulated periodically, and surface species interact with the perturbation at different rates. The spectra can be transformed into the phase domain and the time signature can be expressed as a phase delay. During this transformation, signals from spectator species, which often drown out those of active species, are repressed. The phase delay can be analyzed to determine the behavior of the various visible species and conclusions about activity may be drawn. This experimental method was applied to the methane partial oxidation reaction over ceria zirconia catalysts; methane and oxygen concentration acted as the periodic modulated external stimulus.

3.2 Experimental Methods

Ceria zirconia was synthesized via the ammonium precipitation method [41,49,50]. To wit, cerium and zirconium precursors ($Ce(NO_3)_3 \cdot 6H_2O$, 99% trace metals basis, Sigma Aldrich; $N_2O_7Zr \cdot xH_2O$, 99.99% trace metal basis, Sigma Aldrich) were dissolved in de-ionized water at a Ce:Zr ratio of 3:1. The solution was then added dropwise to a vat of ammonium hydroxide solution. The precipitate was filtered and washed before left to dry in a 105°C oven overnight. The dry precipitate was calcined in air at 450°C for four hours. The calcined material was sieved to a particle size between 75 and 38 microns. To impregnate the nickel and copper, a solution of solvated salts ($Ni(NO_3)_2 \cdot 6H_2O$, 99.999% trace metal basis, Sigma Aldrich; $Cu(CO_3)_2 \cdot H_2O$, 99.99% trace metal basis, Sigma Aldrich) was prepared, the pore volume of the ceria zirconia ascertained, and a solution volume equal to the pore volume was mixed into the powder. This mixture was dried overnight at 105°C. The resultant was calcined at 450°C for four hours.

3.2.1 Physicochemical Characterization

A Micromeritics ASAP 2020 instrument was used for nitrogen physisorption experiments. Approximately 0.6250g of sample was loaded into the sample tube; the tube was degassed at 110°C for 4 hours before analyzing. The surface area was calculated with the BET method [51] and pore volume was determined by the BJH desorption method [52].

XRD spectra were measured with an X'Pert PRO Alpha-1 diffractometer with a copper anode and an X'celerator module. Kα diffractograms were collected over 2Θ positions [20-100] with a step size of 0.0170. The samples were loaded into a 16mm sample holder tray.

To measure Lewis Acidity, pyridine adsorption coupled with FTIR spectroscopy was used. Approximately 20 mg of catalyst was pressed into a wafer and loaded into a vacuum cell. The samples were activated at 450°C for one hour under high vacuum. A spectrum of the clean catalyst surface was collected and then pyridine was dosed repeatedly at 150°C until equilibrium was reached. This was followed by evacuation for one hour. The cell was heated to 250°C, 350°C, and 450°C; in between the temperature spikes, the temperature was lowered to 150°C and spectra collected. Once the wafer was removed, the area which the beam hit was punched out and weighed to allow for the determination of the wafer density.

X-ray Photoelectron Spectroscopy (XPS) measurements were conducted on a Thermo K-alpha XPS. An aluminum K-alpha X-ray (1.486 keV) source was used for excitation. The 72 W X-ray beams was focused to a length of 400μm. High-energy resolution spectra were collected for Ce, Zr, O, Ni, and Cu using a pass energy of 50eV with a step size of 0.10 eV. Powder samples were loaded into cylindrical holes (3 mm diameter, 3 mm deep) on a copper-alloy sample plate. The pressure in the analysis chamber was maintained at less than $2x10^{-8}$ Torr during analysis.

Temperature Programed Reduction was performed on a Micromeritics AutoChem III at the Micromeritics Instrument Corporation site in Norcross, GA. The sample temperature was ramped from 50°C to 900°C at 5 K/min under 20 sccm of 10% H_2 in Argon.

3.2.2 Infrared Experiments

MES experiments are performed on a house-made reaction set-up (See section D.1 in the appendix for exact experimental parameters) and spectra were collected with a Thermo Scientific Nicolet iS20 FTIR Spectrometer. Approximately 30 mg of catalyst was pressed into a self-supported wafer. The wafer was mounted in an IR cell based on that which was described by Wang et. al [53]. The wafer, once loaded, was activated at 450°C for 1 hour under a nitrogen atmosphere before the temperature was lowered to 300°C. The modulation experiments were then conducted at 300°C.

A synopsis of the mathematical formulation for the mathematical treatment may be seen in section D.2. The MES spectra were analyzed with a python script developed by Giada Innocenti in conjunction with the Flaherty group (https://github.com/giadainnocenti/FTIR_analyzer). The code is a python version of the MATLAB code from a recent publication [43]. The reaction was assumed to be reversible and an average was extracted from the periodic concentration cycling. The first few loops (2 for the methane sequences, 5 from the oxygen sequences) were removed since the system had not yet plateaued at a constant average intensity (quasi-steady state). Although the script was constrained to fit up to a maximum of ten phase-shifted spectra, the data were well-described by two. In each case, two functions in the phase domain, 90° out of phase from each other, were used to define each experiment.

3.3 Experimental Results

3.3.1 Physicochemical Characterization Results

Only CZ diffraction peaks are visible in the XRD spectra, as seen in Figure 3.3. 1, due to the dispersion of the dopants and the low concentrations.

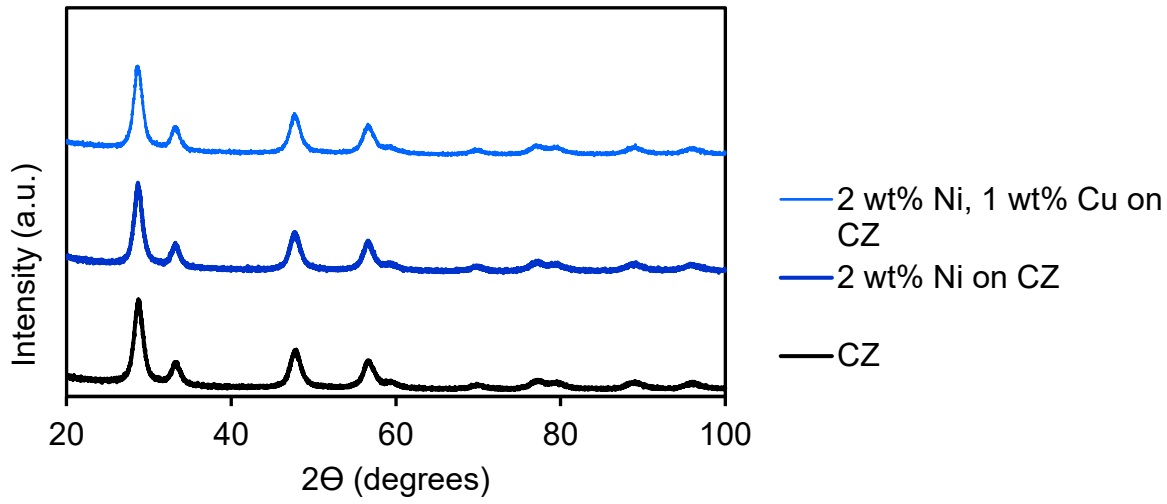

Figure 3.3. 1 XRD patterns of the ceria zirconia support (CZ) and metal oxide impregnated catalysts

Results of other physiochemical characterization, including surface area analysis, pore volume determination, Lewis acidity, and elemental composition, may be seen in Table 3.3. 1.

Table 3.3. 1 Physiochemical characteristics of the ceria zirconia (CZ) support and metal oxide impregnated catalysts

	CZ	**2 wt% Ni CZ**	**2 wt% Ni 1 wt% Cu CZ**
BET Surface Area (m^2/g)[a]	80±6	68±8	69±2
Pore Volume (cm^3/g)[b]	0.12±.02	0.09±0.02	0.09±.01
Lewis Acid Site Concentration (mmol/g)[c]	0.035	0.069	0.105
Ce/Zr ratio[d]	0.42	0.42	0.38

[a] Surface areas calculated using the BET method [51]
[b] Pore volume calculated using the BJH method applied to the desorption isotherm [52]
[c] Measured by pyridine adsorption followed by FTIR spectroscopy at 150°C, assuming a 1:1 pyridine to acid site ratio. Since pyridine will decompose at these temperatures on the ceria zirconia catalysts, the carbonate peak must

be deconvoluted from the pyridine adsorption band [54]. The carbonate peak areas were removed to calculate these reported values.
[d]from XPS measurements

Temperature Programed Reduction (TPR) results for all catalysts may be seen in Figure 3.3. 2. The particles on the surface of the ceria zirconia were more easily reduced than the ceria zirconia support.

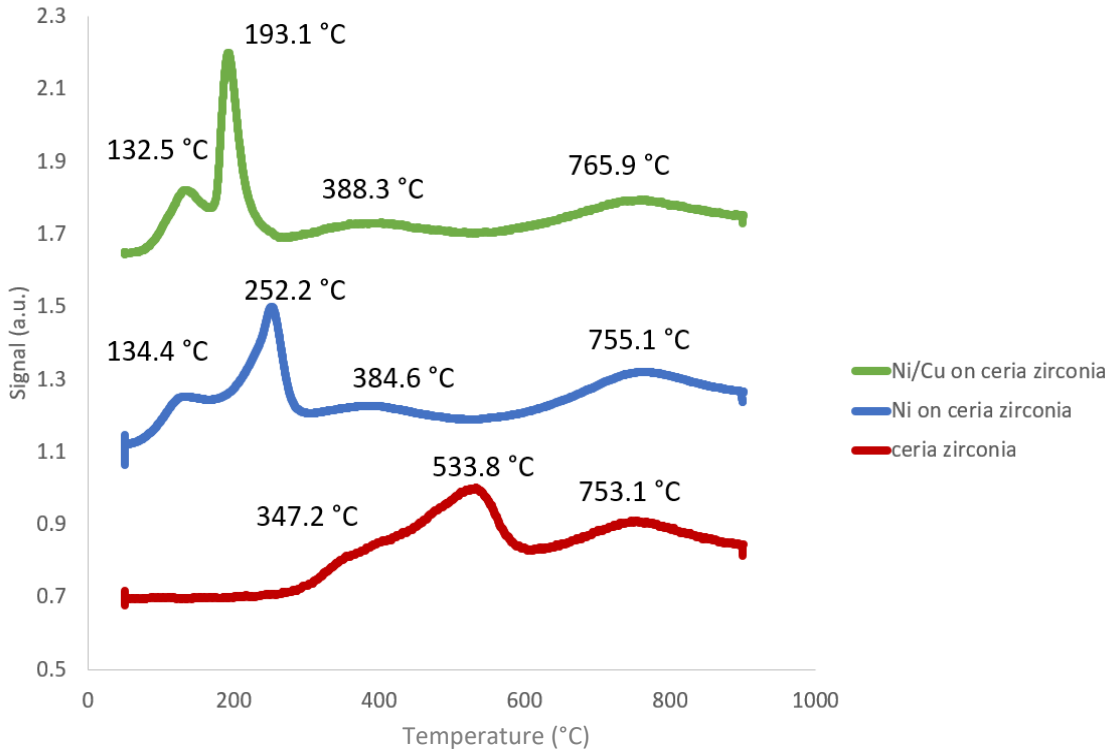

Figure 3.3. 2 TPR curves for ceria zirconia supports and metal oxide impregnated catalysts

The XPS spectra showed copper and nickel peaks, but the quantity was below the quantification limit for the software.

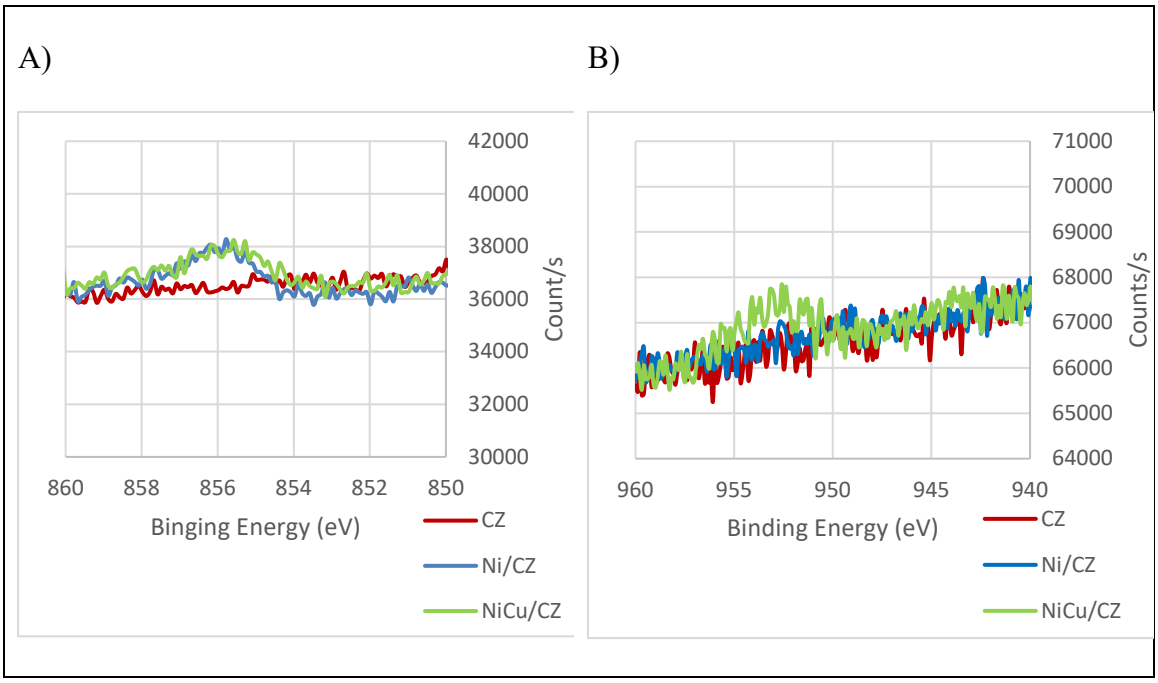

Figure 3.3. 3 A) Ni2p3 (855 eV) for ceria zirconia (CZ), 2 wt% nickel on ceria zirconia (Ni/CZ), and 2 wt% nickel and 1 wt% copper on ceria zirconia (NiCu/CZ) B) Cu2p1 (952) eV for CZ, Ni/CZ, NiCu/CZ

3.3.2 Modulation Excitation Spectroscopy Results

MES phase angle relations for methane modulation may be seen in Figure 3.3. 4-Figure 3.3. 6; oxygen modulation results are shown in Figure 3.3. 7-Figure 3.3. 9. The gas phase methane was subtracted out though the subtraction was more complete in the oxygen modulation experiments (where the methane concentration was constant) when compared to the methane modulation; some methane peaks are still visible in the resulting spectra. For this reason, peak assignments around 3000cm^{-1} are often not listed.

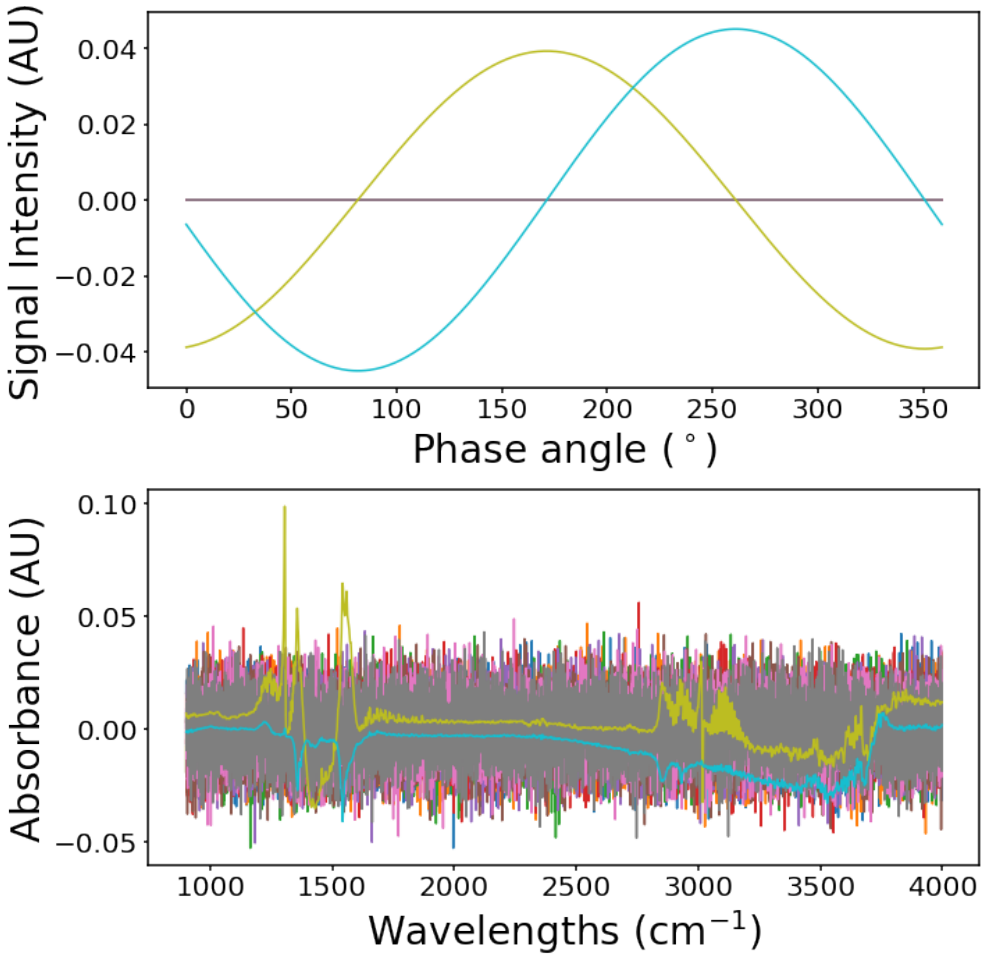

Figure 3.3. 4 Ceria zirconia methane modulation results

Table 3.3. 2 Ceria zirconia methane modulation peak assignments

Color in Figure 3.3. 4	Peak (cm^{-1})	Assignment	Reference
Green	1249	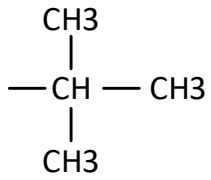	[55]
	1300	Methane	This work
	1357	Formate, ν_{sym}(O-C-O)	[56–59]
	1540	Formate, ν_{asym}(O-C-O)	[56–59]
Blue	1359	Formate, ν_{asym}(O-C-O)	[56–59]
	1425	Aromatic, $\delta(CH_2)$	[60]
	1475	Aromatic, C-C stretch	[61–63]
	1546	Formate, ν_{asym}(O-C-O)	[56–59]
	2855	Formate, ν_{sym}(C-H)	[54,56,57,59,64,65]
	2934	Formate, ν_{asym}(C-H)	[56–58,64,65]

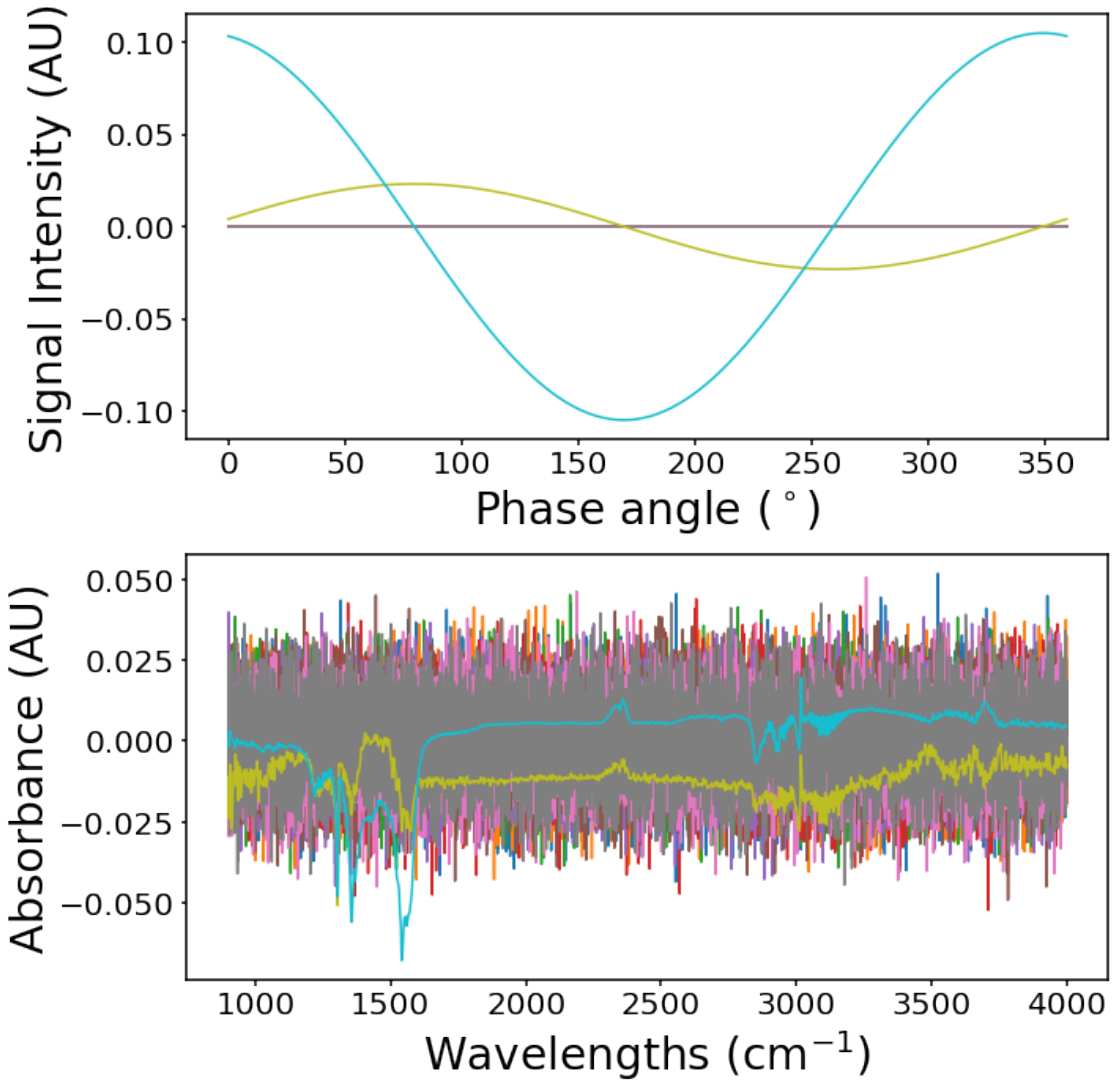

Figure 3.3. 5 2 wt% Ni on ceria zirconia methane modulation results

Table 3.3. 3 2 wt% Ni on ceria zirconia methane modulation peak assignments

Color in Figure 3.3. 5	Peak (cm^{-1})	Assignment	Reference
Green	1231	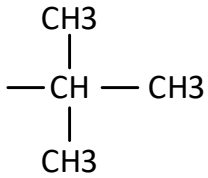	[55]
	1299	Methane	This work
	1357	Formate, ν_{sym}(O-C-O)	[56–59]
	1561	Formate, ν_{asym}(O-C-O)	[56–59]
Blue	1228	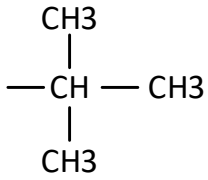	[55]
	1300	Methane	This work
	1361	Formate, ν_{sym}(O-C-O)	[56–59]
	1434	Aromatic, $\delta(CH_2)$	[60]
	1500	C=C aromatic stretch	[66]
	1556	Formate, ν_{asym}(O-C-O)	[56–59]

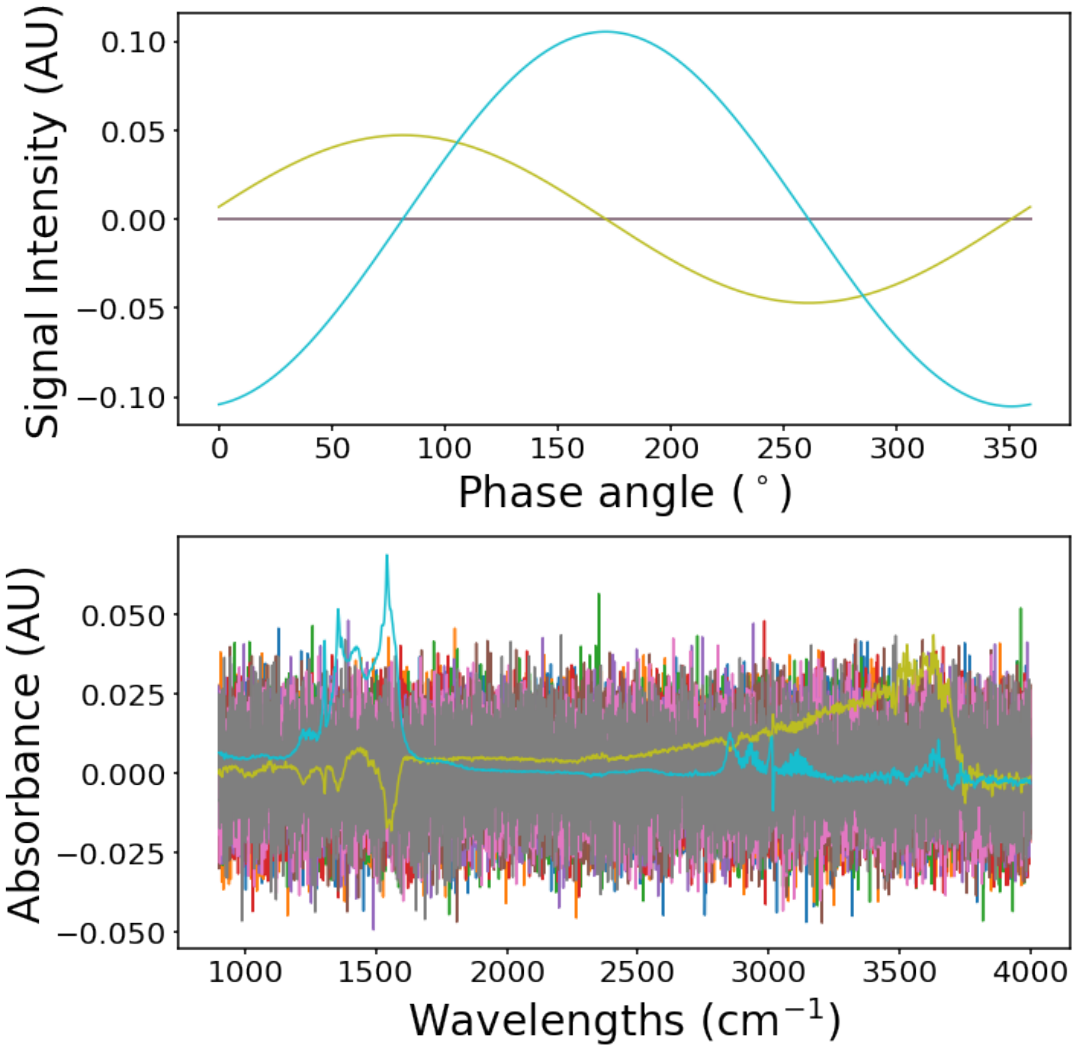

Figure 3.3. 6 2 wt% Ni, 1 wt% Cu on ceria zirconia methane modulation results

Table 3.3. 4 2 wt% Ni, 1 wt% Cu on ceria zirconia methane modulation peak assignments

Color in Figure 3.3. 6	Peak (cm^{-1})	Assignment	Reference
Green	1034	Alkoxy, ν(CO)	[67]
	1233	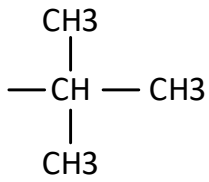	[55]
	1301	Methane	This work
	1360	Formate, ν_{sym}(O-C-O)	[56–59]
	1501	C=C aromatic stretch	[66]
	1553	Formate, ν_{asym}(O-C-O)	[56–59]
Blue	1234	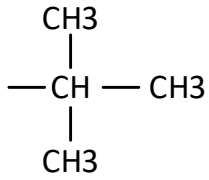	[55]
	1300	Methane	This work
	1359	Formate, ν_{sym}(O-C-O)	[56–59]
	1424	Aromatic, $\delta(CH_2)$	[60]
	1490	C=C aromatic stretch	[66]
	1550	Formate, ν_{asym}(O-C-O)	[56–59]

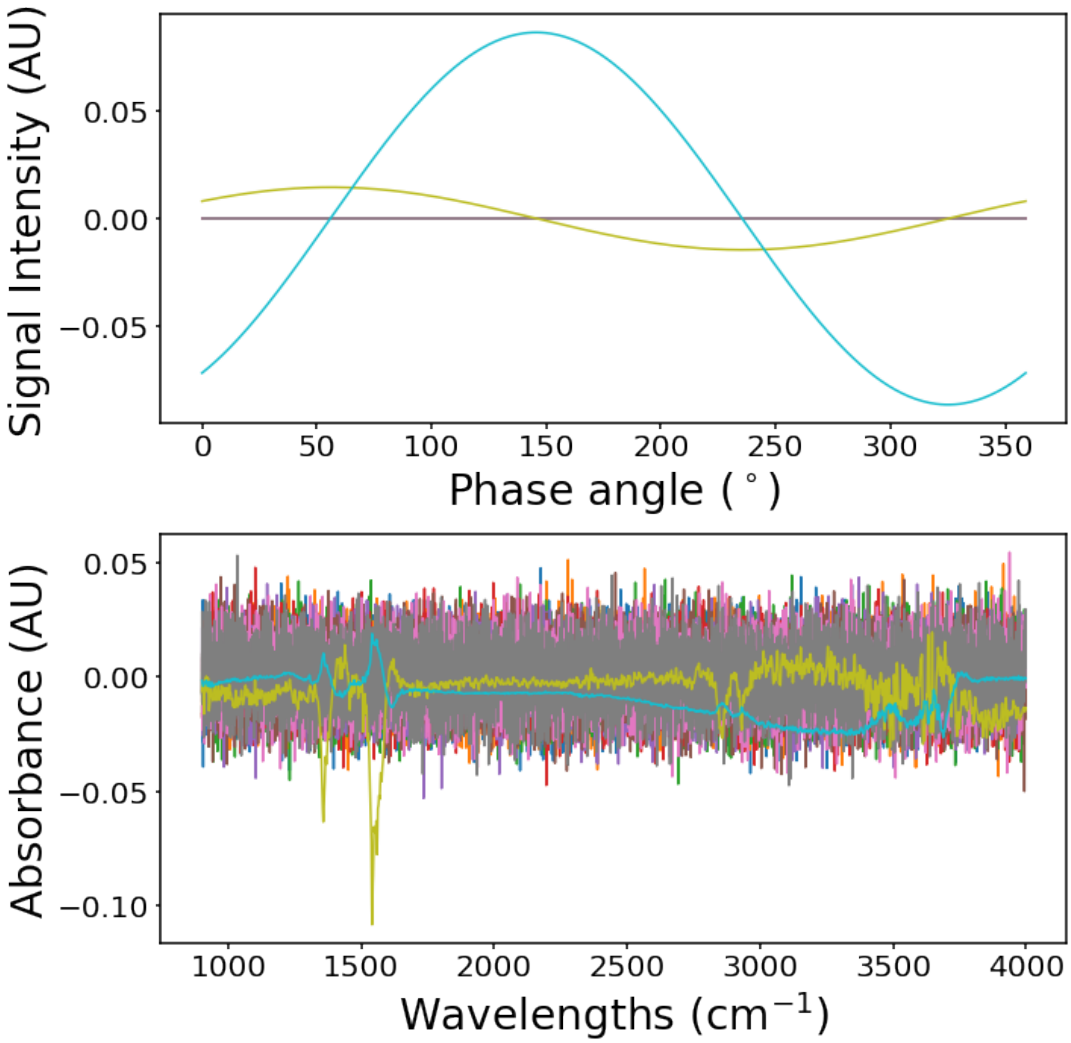

Figure 3.3. 7 Ceria zirconia oxygen modulation results

Table 3.3. 5 Ceria zirconia oxygen modulation peak assignments

Color in Figure 3.3. 7	Peak (cm^{-1})	Assignment	Reference
Green	1360	Formate, ν_{sym}(O-C-O)	[56–59]
	1551	Formate, ν_{asym}(O-C-O)	[56–59]
	2856	Formate, ν_{sym}(C-H)	[54,56,57,59,64,65]
	2931	Formate, ν_{asym}(C-H)	[56–58,64,65]
Blue	1360	Formate, ν_{sym}(O-C-O)	[56–59]
	1551	Formate, ν_{asym}(O-C-O)	[56–59]
	2859	Formate, ν_{sym}(C-H)	[54,56,57,59,64,65]
	2934	Formate, ν_{asym}(C-H)	[56–58,64,65]

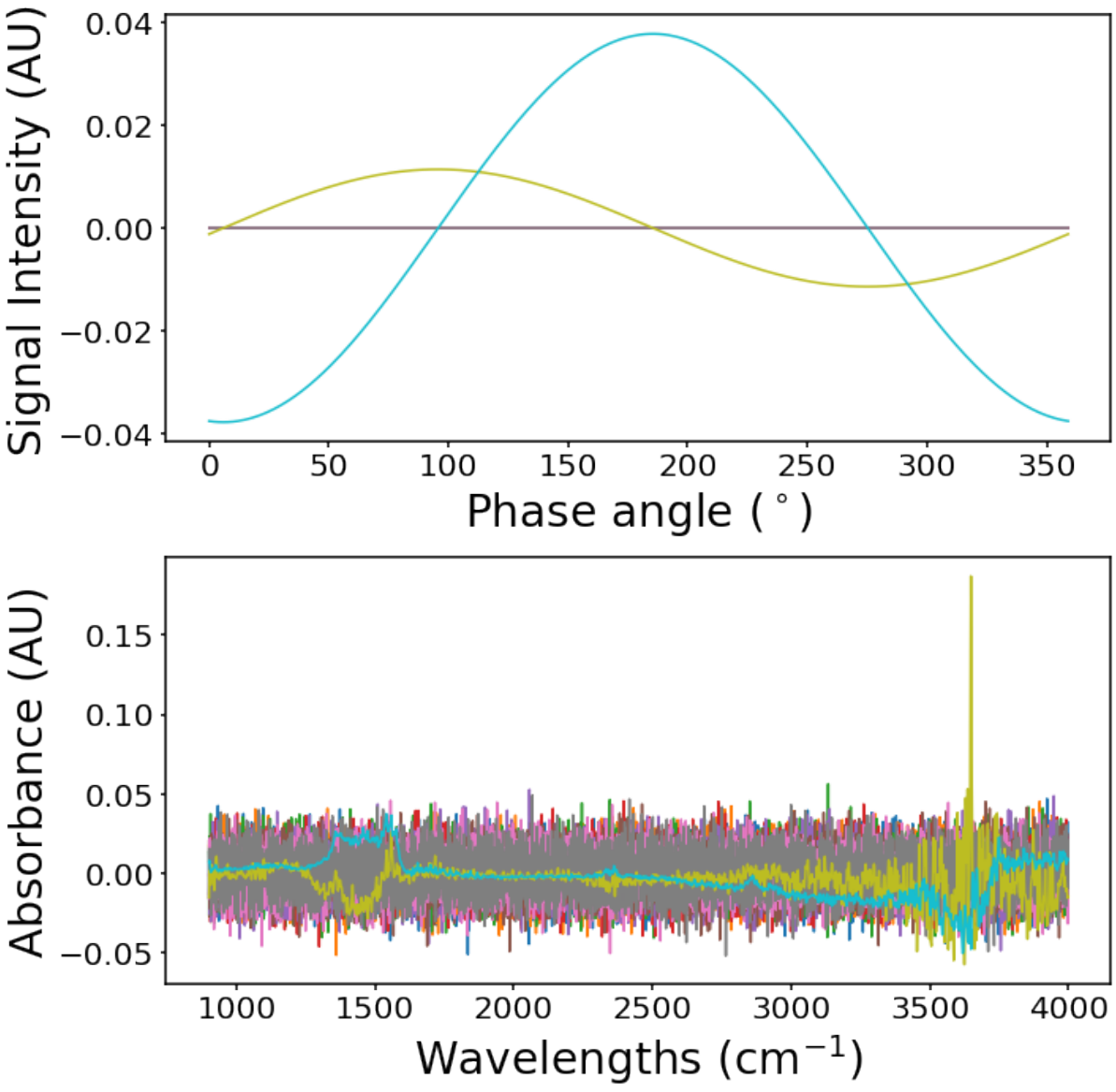

Figure 3.3. 8 2 wt% Ni on ceria zirconia oxygen modulation results

Table 3.3. 6 2 wt% Ni on ceria zirconia oxygen modulation peak assignments

Color in Figure 3.3. 8	Peak (cm^{-1})	Assignment	Reference
Green	1315	Tentatively assigned to cyclopropane	[66]
	1418	Tentatively assigned to cyclopropane	[66]
	1479	Aromatic, C-C stretch	[61–63]
	1575	Tentatively assigned to C=C π interaction with a metal	[66]
Blue	1078	Alkoxy, ν(CO)	[67]
	1148	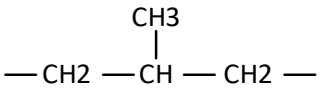	[55]
	1373	Formate, ν_{sym}(O-C-O) (aliphatic)-CH3, sym def.	[56–59] [55]
	1468	(aliphatic)-CH3, asym def.	[55]
	1549	Formate, ν_{asym}(O-C-O)	[56–59]

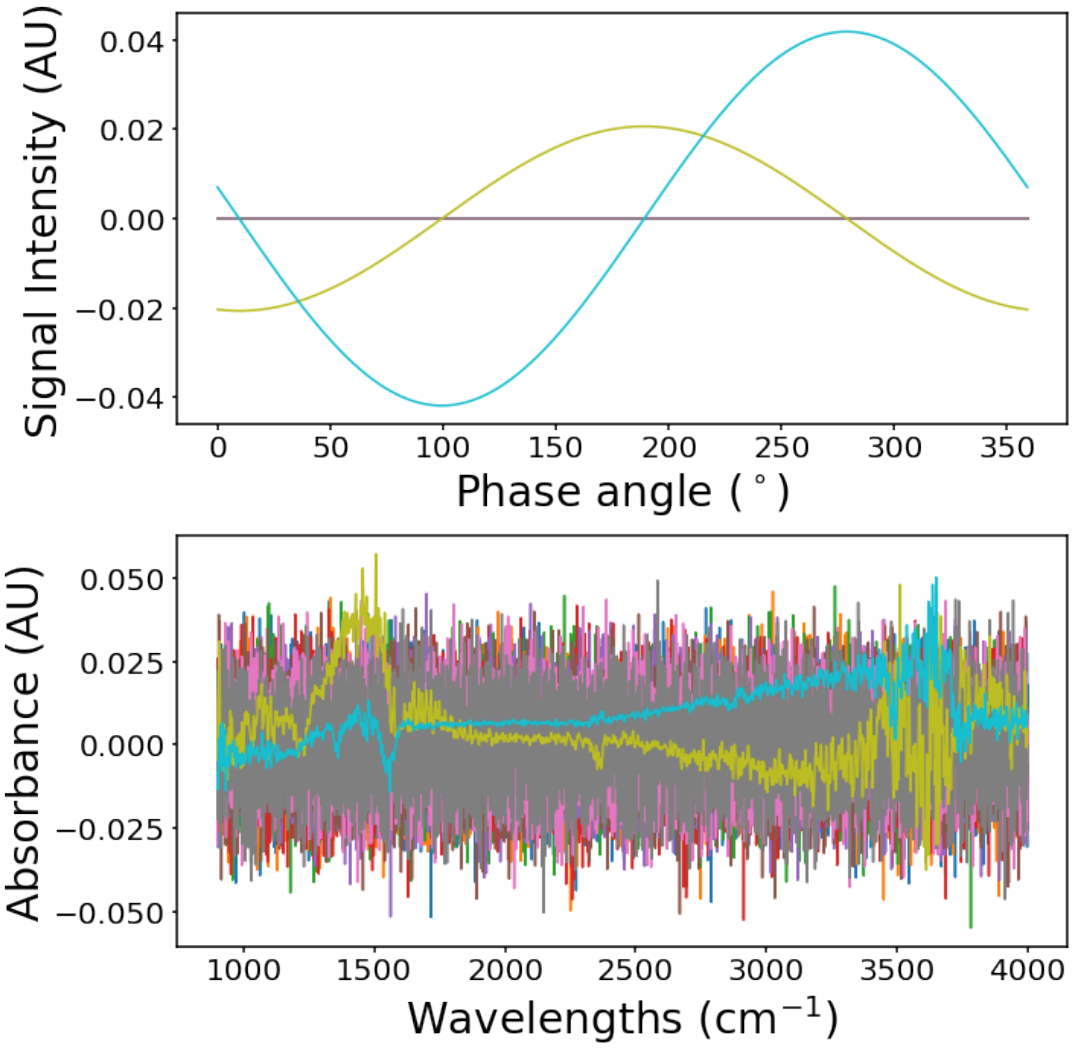

Figure 3.3. 9 2 wt% Ni, 1 wt% Cu on ceria zirconia oxygen modulation results

Table 3.3. 7 2 wt% Ni, 1 wt% Cu on ceria zirconia oxygen modulation peak assignments

Color in Figure 3.3. 9	Peak (cm^{-1})	Assignment	Reference
Green	1066	Alkoxy, ν(CO)	[67]
	1296	Tentatively assigned to cyclobutane	[66]
	1378	(aliphatic)-CH3, sym def.	[55]
	1447	(aliphatic)-CH3, asym def.	[55]
	1512	C=C aromatic stretch	[66]
Blue	1355	Formate, ν_{sym}(O-C-O)	[56–59]
	1553	Formate, ν_{asym}(O-C-O)	[56–59]

3.4 Discussion

Formates were formed, and consumed, in every set of phase-domain spectra. It has been postulated that formates and carbonates are the precursors to carbon dioxide [42], the complete combustion product which competes with any methane partial oxidation reaction. The formates, then, are an active species in this reactive system; however, they are likely not an active species in the reaction of interest, i.e. methanol production. Aromatic and aliphatic bands featured often as well. It has been hypothesized that these species are

necessary to passivate overly-active sites which facilitate CO_2 formation [41]. These bands are actively increasing and decreasing in intensity through the course of the experiment and so are not spectator-species. Though they are active, it is likely that these species only indirectly lead to the selective oxidation products desired. Surprisingly, active alkoxy species—assumed precursors to methanol production—were only detected on the nickel/copper catalysts. It has been reported that the addition of copper electrically modifies the nickel particles by making electron transfer easier and reduces particle size [68,69]. The change in surface characteristics seems to induce the production of the desired surface species. The observation that these species only appear on nickel/copper catalysts is surprising due to others' observations that methanol may be produced over nickel on CZ catalysts in addition to nickel/copper ones [41]. It may be that methanol is produced via another mechanism in that case.

The formates and the alkoxy species formed during the oxygen modulation over the 2 wt% Ni, 1 wt% Cu on CZ exhibited different phase delays. Since these species are not forming together, there should be a specific timed sequence to maximize yield to the alkoxy species and reduce production of formates. Chemical looping would be an appropriate reaction engineering method for this catalyst, given these results. Chemical looping has been applied to methanol production from methane over iron and copper zeolites, though often a temperature swing is added, e.g., the catalyst is activated at about 450°C under oxygen, the temperature is lowered to around 200°C, and then methane is fed in an anaerobic environment. This process is then repeated [30,31,33,70–72]. The results discussed in this work provide evidence that isothermal chemical looping could still be viable, since all of these experiments were conducted at a constant temperature of 300°C.

Cyclic stresses fatigue physical materials and fatigue is estimated to cause 90% of all metallic failures [73]. In addition to drastically reducing the life cycle of operating equipment, this technique can become very expensive. CO_2 sorption via pressure swing adsorption is hampered by the same economic constraints: the energy associated with the temperature or pressure swing escalates costs [74]. The profit margin separating methane from methanol is insufficient to cover this energy input. A few researchers have studied isothermal chemical looping for methanol synthesis: Tomkins et. al. studied copper exchanged zeolites and found that the elevated methane pressure (up to 36 bar) allowed for isothermal methanol production [75]. Sushkevich and van Bokhoven studied isothermal methanol production over several copper exchanged zeolites (MFI, MOR, BEA, FAU) and found that over the faujasite zeolites, assumed to be inactive, methanol could be isothermally synthesized [76]. Copper exchanged erionite zeolite will also yield methanol from direct isothermal methane oxidation [77]. Periodic or transient control has also been used to enhance catalytic combustion of methane over ceria catalysts in the context of exhaust cleaning; under these dynamic conditions, the methane alternates between total and partial oxidation [78]. Isothermal chemical looping should improve methanol yield over the nickel/copper doped CZ.

3.5 Conclusions

Infrared (IR) spectra were collected over three catalysts: ceria zirconia (CZ), 2 wt% nickel on CZ, and 2 wt% Ni, 1 wt% Cu on CZ. All three catalysts were subjected to methane modulation and oxygen modulation sequences and the formation of actively changing surface species was induced. Formates were common across all experiments, highlighting the ubiquity of carbon dioxide formation in methane partial oxidation reactive

systems. Alkoxy species modulated synchronously with aromatic/aliphatic groups; these species compete with each other during methanol production over ceria zirconia catalysts. The formates modulate out of sync with the alkoxy species during the oxygen modulation experiments, and so chemical looping, where the oxygen concentration is the controlled variable, may be a promising reaction engineering approach for increasing yield in this system.

More information about the kinetic parameters of individual species could be gathered from the repetition of these experiments at a series of other frequencies [46]. Computational methods would help confirm infrared assignments too. A faster sampling time with the infrared spectrometer may elucidate other shorter-lived species which escaped observation with this experimental setup.

CHAPTER 4. WATER SPLITTING VIA MECHANOCHEMICAL METHODS

4.1 Introduction

Mechanochemistry usually refers to any chemical reaction induced mechanically [79,80]. Mechanochemical systems allow for solvent-free (in that no solvent was intentionally added) or reduced-solvent syntheses, reducing cost and energy input [79]. Mechanical impact can result in physicochemical changes to a catalytic material; these effects include improved diffusion, improved contact between multiple phases, introduction of strain, structural, and electronic defects, as well as local pulses of temperature and pressure [80–82]. Ball milling, wherein catalysts and reagents are loaded inside a vessel with spherical milling media, has become a standard technique to carry out mechanochemical reactions [83]. In ball mills, it is theorized that collisions of the balls result in brief hot spots of very high, localized temperature [79,80,84,85]. These hot spots allow reactions of interest, usually requiring high temperature and/or pressure, to proceed at nominally ambient conditions (though it has been noted that the mechanical actions can induce substantial temperature effects inside the ball milling vessel [86]). Hot spots, existing for mere milliseconds, may reach temperatures exceeding 1000 K [84].

Two step solar thermal water splitting requires activation of a metal oxide at temperatures upwards of 1400°C [9] and low oxygen partial pressure [87]. The activated form of the metal oxide, with oxygen vacancies produced by the release of oxygen [11],

can then react with steam at a lower temperature (700-1000 °C) to produce hydrogen [9,88]. Solar energy can be concentrated by several means, such as heliostat fields and parabolic dishes, and can be used to reach such temperatures [87]. Ceria (CeO_2) is capable of splitting water using this type of cycle [9–11,88–90]. Because of the stable cubic fluorite structure [11,88,91], ceria circumvents issues like sintering common with other materials [9].

Several materials, when exposed to mechanochemical forces in ball mills, can produce hydrogen from water, materials including quartz powder [12], nickel and chromium together (originally, it was noted that SUS304 could produce hydrogen from water; later the active components were narrowed) [13–15], iron oxide [16], and aluminum powder [17]. A program was developed to ascertain whether ceria might also be able to do so.

4.2 Experimental Methods

Ceria (Cerium (IV) oxide, >99.0% purity) was purchased from Sigma Aldrich. Ultra-High Purity argon gas, as well as the gases used for calibration of the mass spectrometer (UHP oxygen, UHP hydrogen), were purchased from Airgas.

Nitrogen Physisorption experiments were conducted in a Micromeritics ASAP 2020 instrument. The sample was degassed at 110°C for 4 hours before analyzing. The surface area was calculated with the BET method [51] and pore volume was determined by the BJH desorption method [52].

X-ray Diffraction (XRD) spectra were collected via an X'Pert PRO Alpha-1 diffractometer with a copper anode and an X'celerator module. A step size of 0.0170 was used to collect Kα diffractograms over 2Θ positions from 20-100. To quantify the crystallinity of the samples, 10 wt% Lanthanum Hexaboride (LaB6) was mixed into the sample (homogenized for 10 minutes) and XRD spectra were again collected. Based on the LaB6 percentage recorded, the approximate ceria amorphous content could be calculated.

X-ray Photoelectron Spectroscopy (XPS) measurements were conducted on a Thermo K-alpha XPS. A focused monochromatic aluminum K-alpha X-ray (1.486 keV) source was used for excitation. Spectra were collected for Ce, Zr, O, C, and Fe using a pass-energy of 50.0 eV with a step size of 0.10 eV. Data analysis was performed using the Avantage software package, v.5.957.

Samples were shipped to Elemental Analysis, Inc. for Proton Induced X-ray Emission (PIXE) analysis.

Thermogravimetric analyses (TGA) were performed on two machines. Low temperature (up to 900°C) tests were conducted on a TA Instruments SDT Q600 Thermogravimetric Analyzer. 5-10 mg of sample was loaded for analysis. The sample was heated to 30°C and held for 15 minutes to equilibrate, both steps occurring under 20 sccm nitrogen. The sample temperature was then increased to 900°C at 10°C/min under 20 sccm air. To determine behavior of reduced ceria above 900°C, the sample was loaded into a Netzsch STA 449 F3 Jupiter Water vapor furnace which could achieve temperatures up to 1250°C. The sample temperature was increased from 100°C to 1100°C at a ramp rate of

20 °C/min under 20% O_2 in Ar, then held at 1100°C for 30 minutes before cooling back to room temperature.

Scanning Transmission Electron Microscopy (STEM) images were captured on a Hitachi HD-2700, with a 200 kV, spherical aberration (Cs) corrected cold field emission source, and an attached EDS for elemental analysis.

A Retsch Mixer Mill MM500 Nano was used for ball milling experiments. Images of the setup may be seen in Appendix B. 10 g of ceria was loaded into the vessel, with and without 1 mL of water. The headspace was purged with flowing argon and then the milling frequency was increased from 5 Hz to 35 Hz at 5 Hz intervals, increased every 30 minutes. The effluent was analyzed with a Hiden HPR-20 QIC Benchtop Gas Analysis System, Model No. HAS-301-1273.

4.3 Experimental Results

Surface area, pore volume, crystallite size, Ce:O ratio and iron content may be seen in Table 4.3. 1.

Table 4.3. 1 Physicochemical characteristics of the ceria, before and after ball milling

	Ceria	Ceria ball milled in the absence of water	Ceria ball milled with 1 mL water
BET Surface Area (m^2/g)[a]	8.7	4.9	29.4
Pore Volume (cm^3/g)[b]	0.050	0.015	0.061
Crystallite size (nm)[c]	8.2	3.0	3.3
Ce:O ratio (mol/mol)[d]	0.42	0.35	0.38
Iron content (wt%)[e]	0	8.285	2.216

[a] Surface areas calculated using the BET method [51]
[b] Pore volume calculated using the BJH method applied to the desorption isotherm [52]
[c] Calculated using the Scherrer equation for the peak at 28.5°, assuming spherical crystallites.
[d] As determined from XPS measurements.
[e] from PIXE analysis

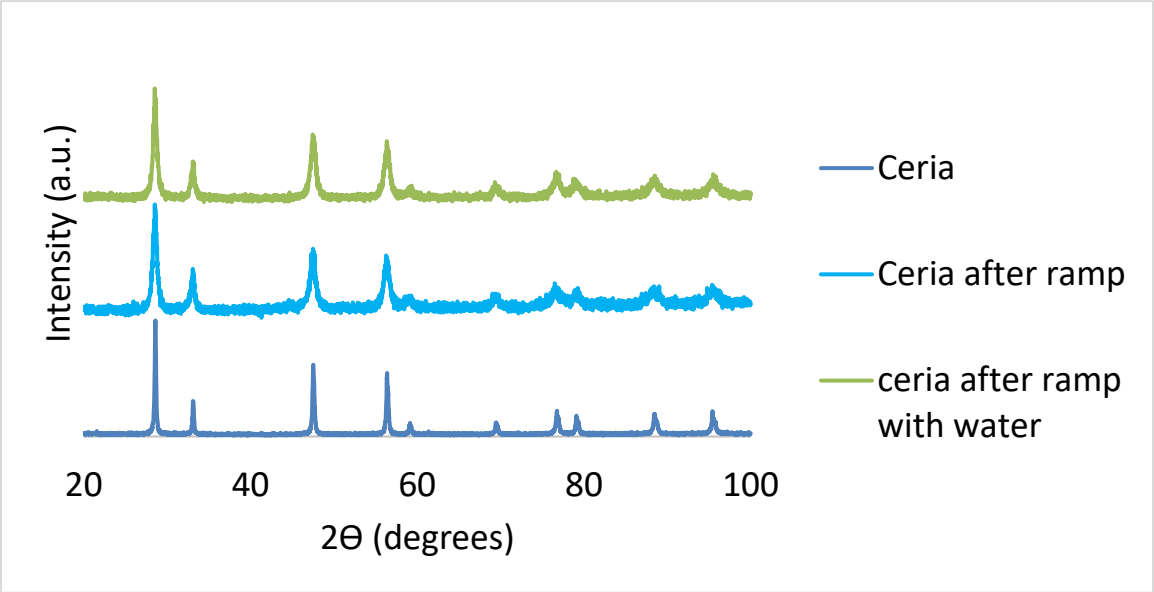

Figure 4.3. 1 XRD spectra of fresh ceria, ceria milled in Ar, and ceria milled in Ar with water

The XRD spectra showed only peaks associated with ceria, though the milled samples were highly amorphized.

Table 4.3. 2 Approximate amorphous ceria content

Material	Approximate amorphous ceria content (%)
Ceria	28
Ceria milled in Ar	85
Ceria milled in Ar with water	79

Ball milling resulted in significant morphological changes. The ceria before milling appeared to have a porous, hollow structure. After milling, smooth surfaces were roughened, and particle size decreased dramatically as seen in Figure 4.3. 2.

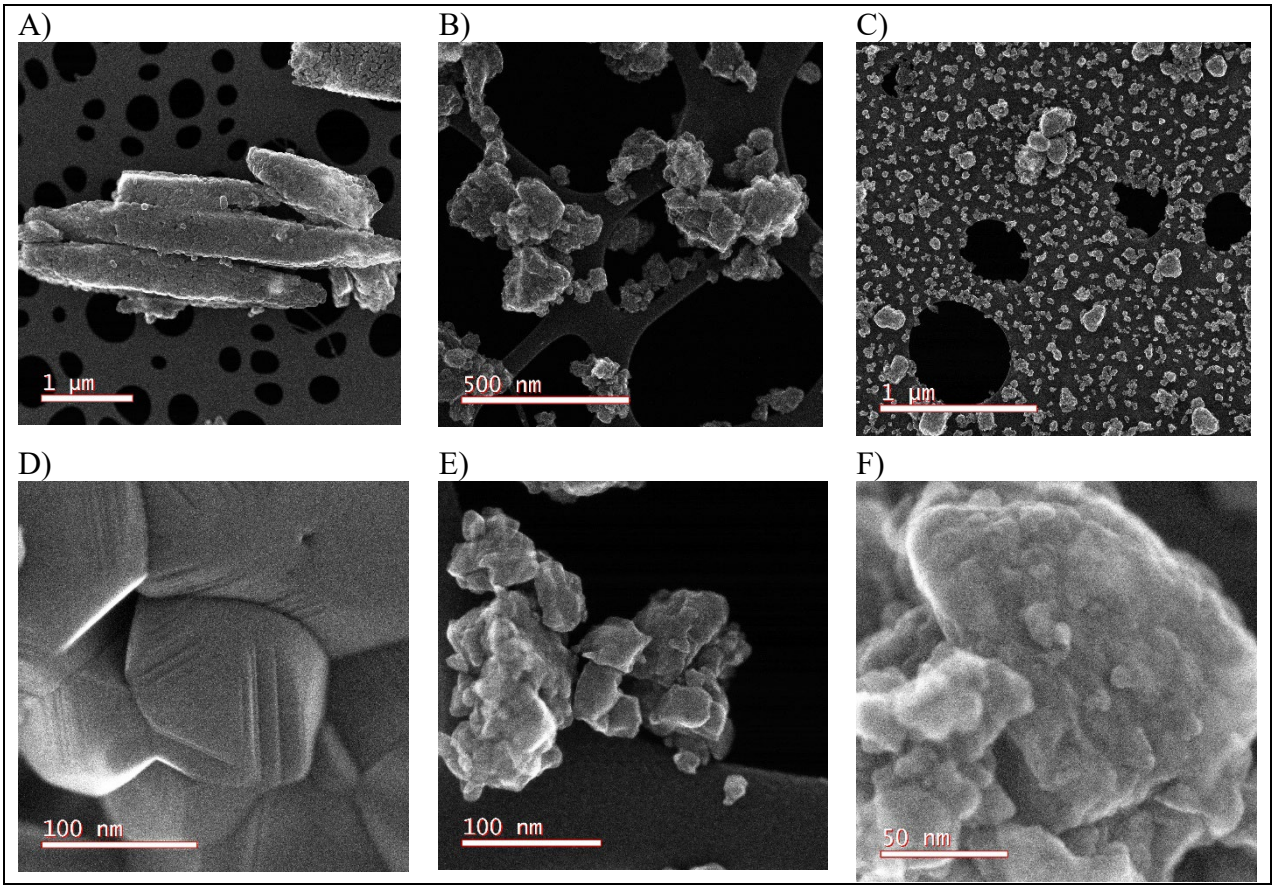

Figure 4.3. 2 A) Ceria before milling B) Ceria milled in Ar C) Ceria milled in the presence of water D) Ceria before milling E) Ceria milled in Ar F) Ceria milled in the presence of water

Material	No. Particles analyzed	Mean (nm)	Median (nm)	Mode (nm)
Ceria	13	1720	1550	1800
Ceria milled in Ar	26	175	172	250
Ceria milled in Ar with water	32	73	65	60

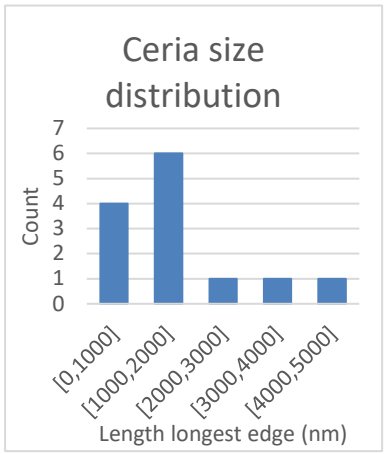

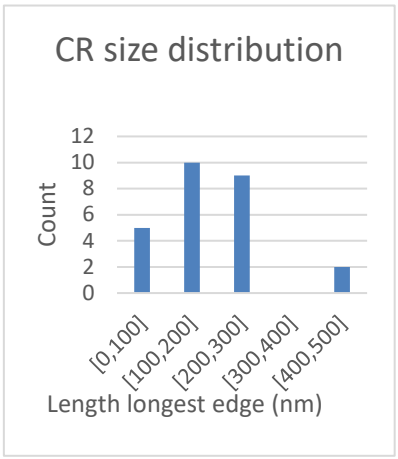

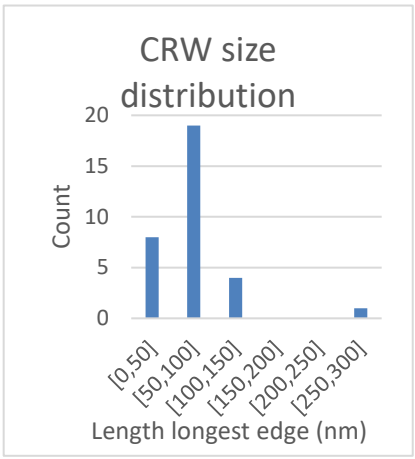

Figure 4.3. 3 Particle size distribution from STEM-EDX imaging

EDS analysis was also performed during the STEM imaging to determine if discernible quantities of iron were present. The iron peak at 6.401 keV overlaps with ceria peaks, so the peak at 7.060 keV was used for analysis. In most of the images, the iron peak was absent, as may be seen in Figure 4.3. 4.

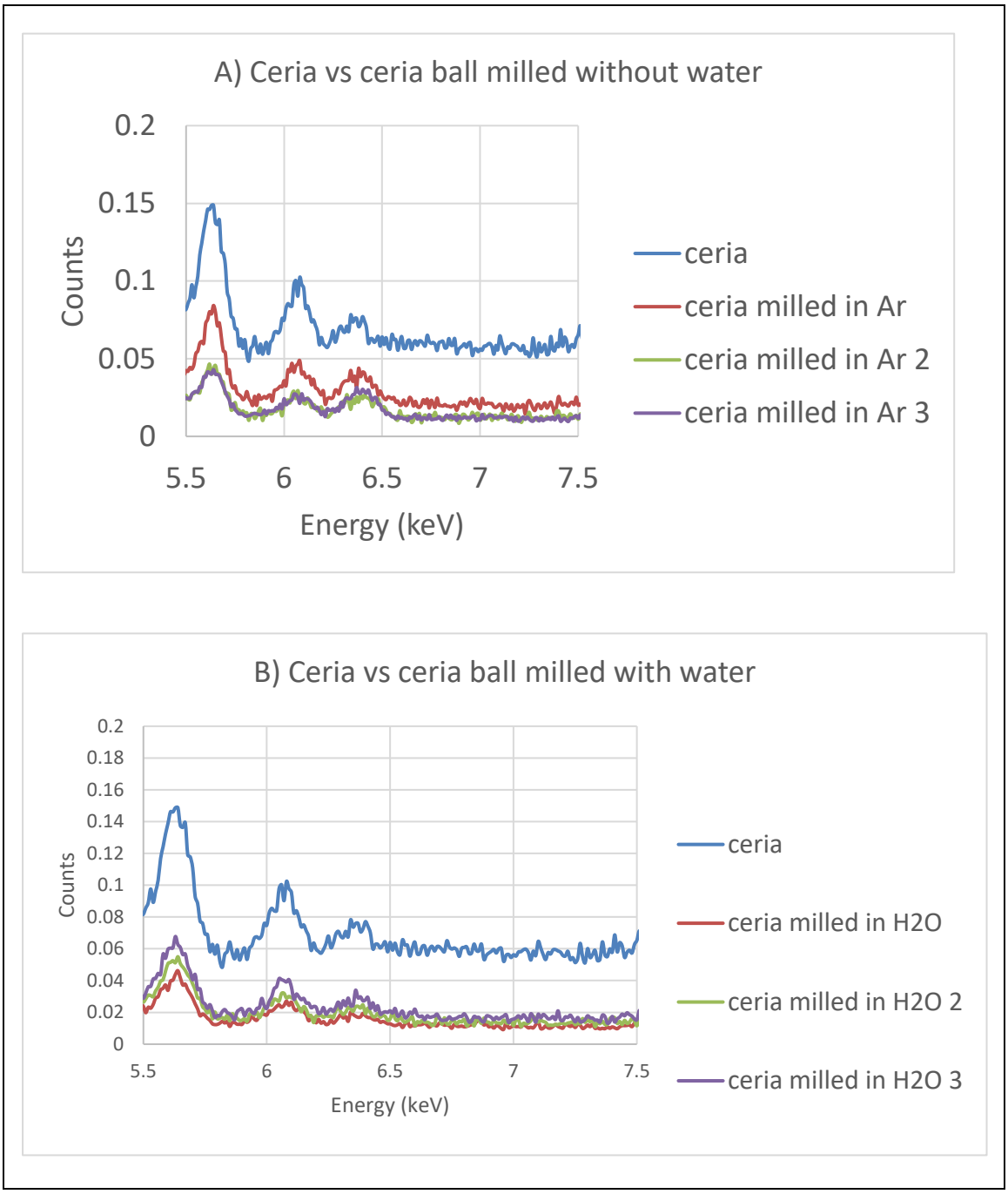

Figure 4.3. 4 A) EDS spectrum of ceria, compared to the ceria which was ball milled without water B) EDS spectrum of ceria as compared to the ceria which was ball milled with water

However, in one image a clear clump of iron oxide was visible.

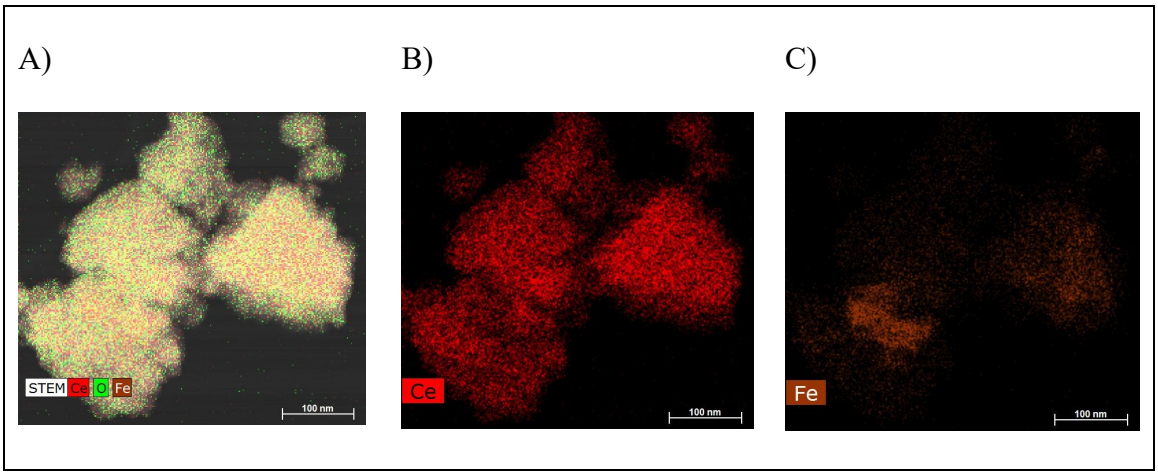

Figure 4.3. 5 STEM-EDX imaging of ceria ball milled in argon. A) composite image with cerium, oxygen, and iron B) cerium scan alone C) iron scan, showing iron oxide clump

The hydrogen evolution followed the changes in milling frequency, increasing with increasing frequency, as seen in Figure 4.3. 6.

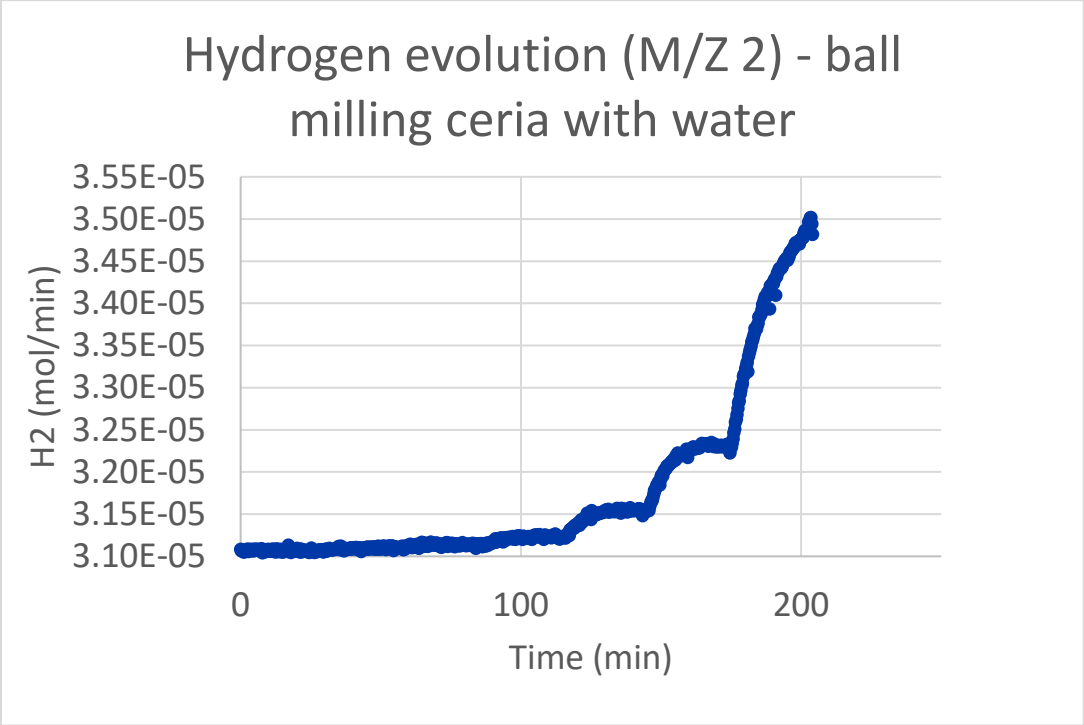

Figure 4.3. 6 Hydrogen evolution when ceria is milled in the presence of water

The milled sample seemed to be still oxidizing at the maximum operating temperature of the TGA (Figure 4.3. 7 A), as shown by the positive slope at 900°C. A higher temperature test was performed (Figure 4.3. 7 B) and the weight increase due to oxidation seemed to cease at 1030°C.

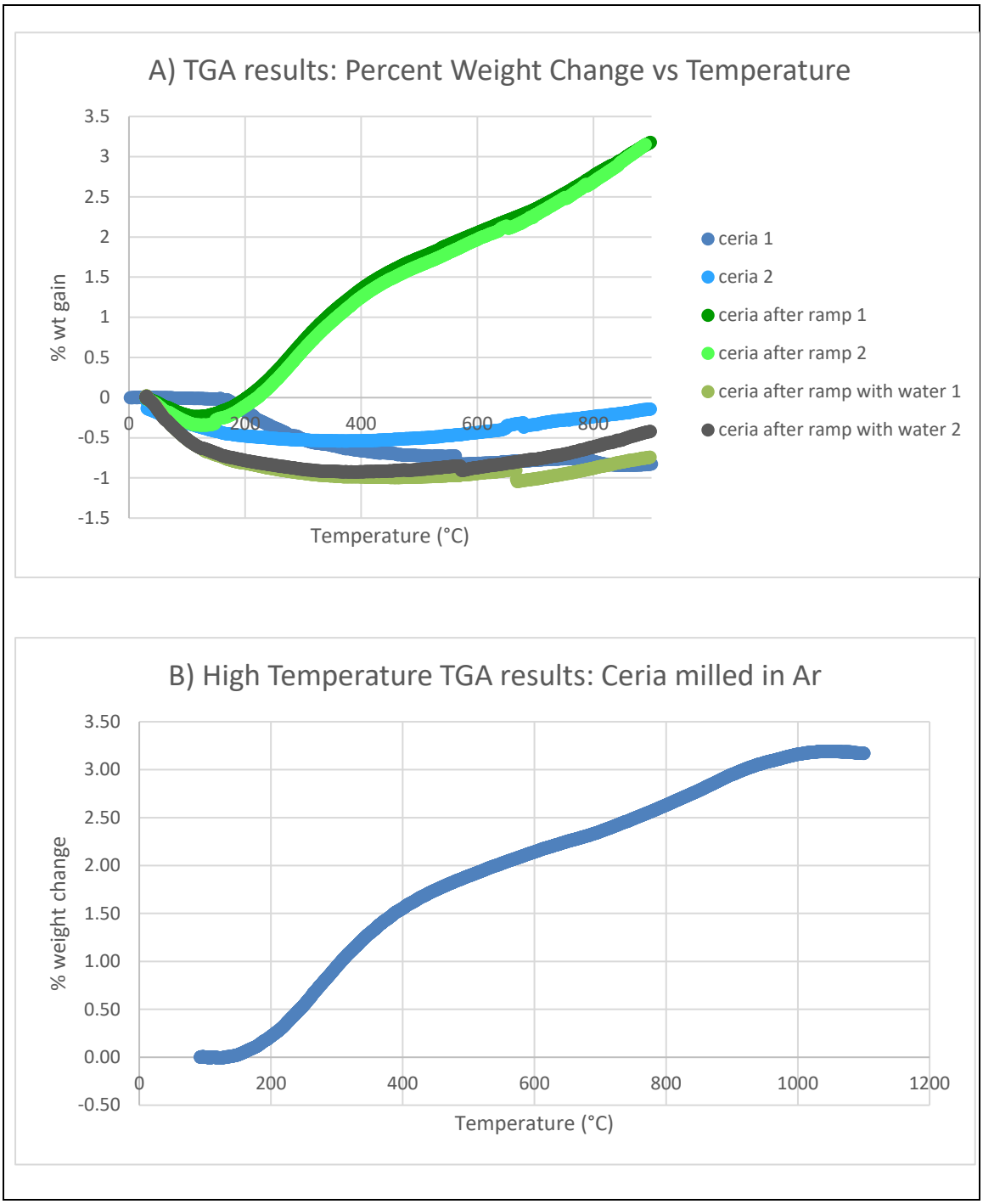

Figure 4.3. 7 Figure C.2. 7 A) Low temperature TGA results B) High temperature TGA results

4.4 Discussion

Hydrogen evolution was observed from the experiments with water and the quantity increased with increasing milling frequency. It was proposed that during milling, oxygen would be forced from the lattice; when the resultant powder was heated under an atmosphere of dry air, oxygen was available to re-enter the material. This oxidation was observed as a weight gain of about 3 wt% in TGA experiments. The powder which was milled in the presence of water lost weight, presumably water, in much the same manner as the original ceria. These results seemed to suggest that the ceria was reduced with milling and returned to its original oxidized state when oxygen from water was present, thereby releasing hydrogen.

The color of the ceria changed dramatically with milling, turning from pale yellow to black. The colorant for mars black, an industrially produced pigment, is iron oxide and it has been shown [13–16] that iron oxide can split water. The vessel and balls were steel and might have induced the reaction. XRD spectra of the ball milled samples show only ceria peaks, but this may only indicate that the quantity was below the detection limit of the machine or that it was not in a crystalline structure. XPS did not resolve iron, but again this may have been because the iron content was less than 1 mole %, the lower detection limit of the instrument, or that the small sample quantity was not representative of the whole sample. The particles were imaged with STEM-EDS. The average particle size decreased and the surface was considerably roughened with milling. Most of the EDX images showed no, or very disperse, iron content; one image did show a large clump of iron oxide. To determine how prevalent the iron, PIXE analysis was completed. The iron content was sufficient to explain the hydrogen production and TGA weight gain (see

Appendix C, equations C1-C10). The ceria, harder than steel, was shaving off material and that material was catalyzing the water splitting reaction.

4.5 Conclusions

Ceria was milled in the presence and absence of water. Initial results suggested that ceria might be responsible for splitting the water and releasing hydrogen. Subsequent tests suggested that, rather than ceria, iron was responsible. Given ceria's interesting physical properties—and its proven capacity to perform the water splitting reaction—mechanochemistry should be an applicable reaction engineering approach should a harder vessel, perhaps zirconium oxide or tungsten carbide, be utilized.

CHAPTER 5. SELECTIVE OXIDATION OF HEPTANE VIA MECHANOCHEMICAL METHODS

5.1 Introduction

It has been postulated that certain hydrocarbon oxidation reactions which usually require high temperature and or pressure might be performed in a ball mill. At hot-spots, conditions of high temperature and pressure conditions exist even when the rest of the vessel is at nominally ambient conditions [84]. It is conceivable that oxygen which is removed from a catalyst's lattice—especially ceria's cubic fluorite structure which releases oxygen so readily [88,92–95]—could enter a hydrocarbon chain and form an oxygenated product or a smaller chain by oxidative cleavage.

5.2 Experimental Methods

Ceria zirconia was synthesized via the ammonium precipitation method (for a detailed description of the method, see section 3.2).

A Retsch Mixer Mill MM400 was used for these experiments. Images and diagrams may be found in Appendix B. For each experiment, the vessel was loaded with approximately 2g of sample and 10 stainless steel balls. Heptane (99% pure, Sigma Aldrich) was chosen as a model condensable hydrocarbon due to its lack of carcinogenicity. Enough heptane was initially added to fill the pore volume of the ceria zirconia catalyst (about 0.3 mL). The headspace was purged with argon and then the milling frequency was set to 15 Hz and the time was set to 90 minutes. For a three hour

test, the mill was restarted after 90 minutes elapsed. A Hiden HPR-20 QIC Benchtop Gas Analysis System, Model No. HAS-301-1273 was used to analyze the effluent.

The surface species present on the spent catalyst powder were observed using a Smart iTR add-in on a Thermo Fischer Nicolet is20 infrared spectrometer.

To determine how the mechanical-chemical action affected the surface reduction, XAS spectra were recorded at the synchrotron at Brookhaven National Laboratory. The samples were unloaded from the MM400 vessel under argon and then loaded into the sample tray for analysis under an inert atmosphere in a glove box.

5.3 Experimental Results

Spectra were collected of the fresh ceria zirconia, the milled ceria zirconia, and the ceria zirconia which was milled in the presence of heptane. Figure 5.3. 1 shows the peaks which arise from milling with heptane (the ball milled ceria zirconia features have been subtracted out).

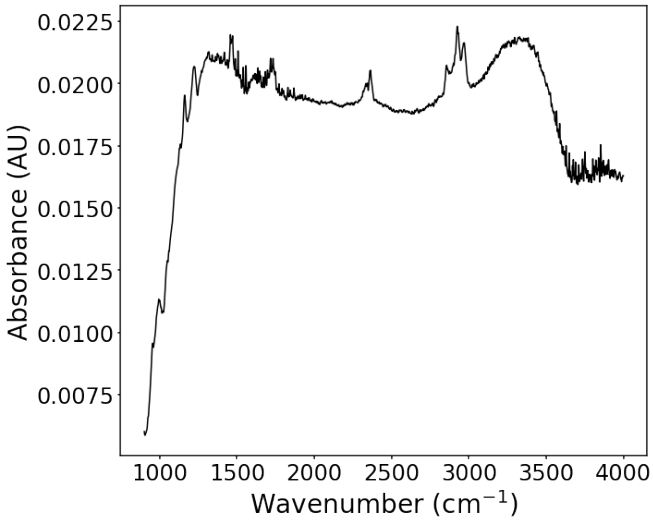

Figure 5.3. 1 Infrared spectrum of ceria zirconia milled with heptane with milled catalyst features subtracted out, recorded from 900-4000cm-1

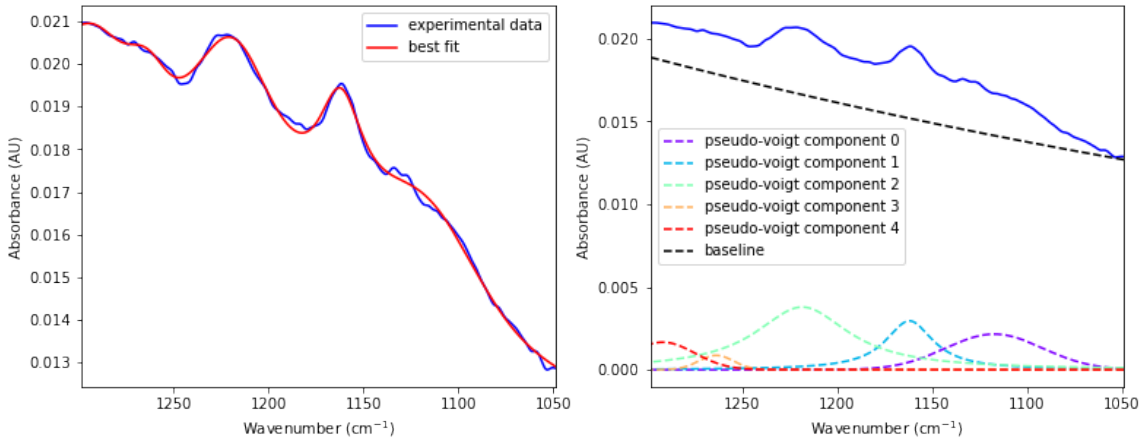

Figure 5.3. 2 Infrared spectrum of ceria zirconia milled with heptane (milled catalyst features subtracted out), with deconvoluted peaks, 1050-1300cm-1

To determine if the features observed were due only to physisorption of heptane, an experiment was conducted wherein ceria zirconia was loaded into the ball mill with heptane

(without any milling balls) and argon was passed through the setup (with the shaker mill operating) for three hours. The surface of the ceria zirconia after the shaking treatment showed different features than the surface after the milling treatment as the subtraction spectrum Figure 5.3. 3 in shows.

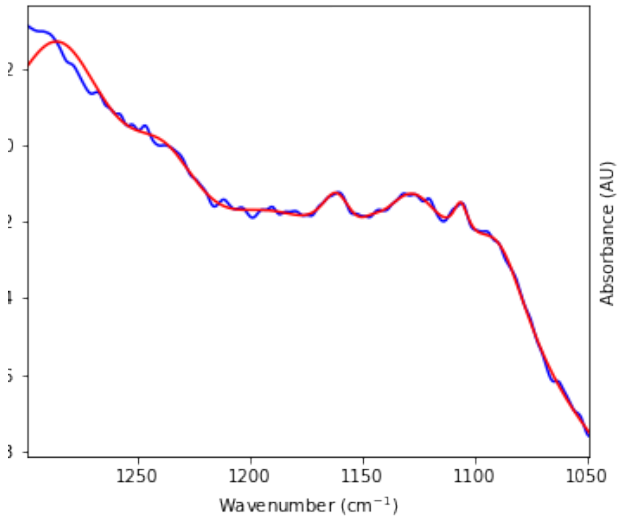

Figure 5.3. 3 Ceria zirconia ball milled with heptane with the heptane physisorption features (from shaking treatment) subtracted out

Table 5.3. 1 Possible oxidation product peak assignments on ceria zirconia after ball milling with heptane

Peak position (cm^{-1})	Assignment	Reference
1221	C-O-C asymmetric stretching of saturated aliphatic esters or C-O stretching for aliphatic tertiary alcohols	[66]
1161	C-O-C asymmetric stretching for saturated aliphatic ethers or C-O-C symmetric stretching of ester. Might also be C-C stretching of isopropyl compound.	[66]

Additional experiments, such as catalyst washing followed by GC analysis, should be performed to confirm or refute these assignments.

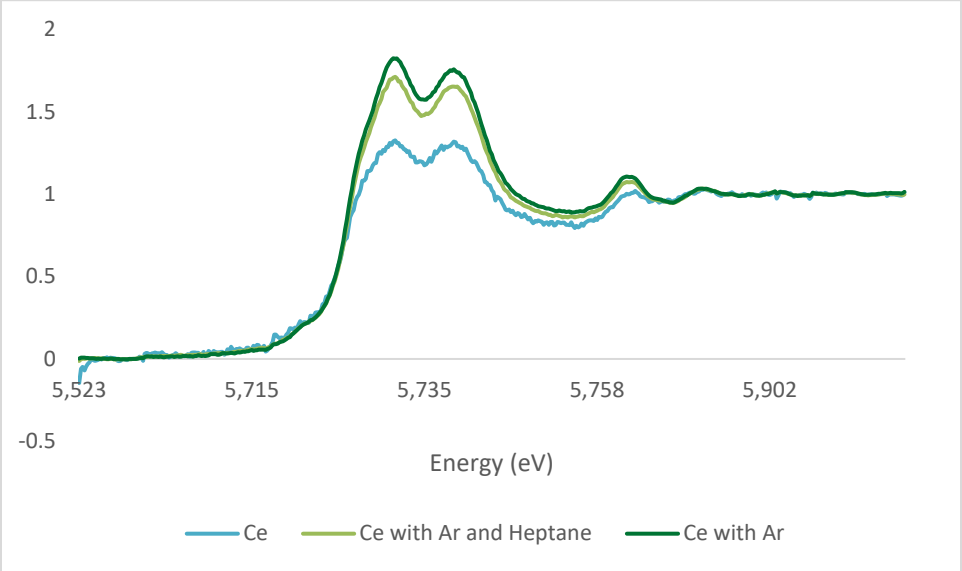

Figure 5.3. 4 X-ray adsorption near-edge spectroscopy (XANES) spectra for milled ceria samples, relative to a control

The XANES features do not exhibit substantial signs of reduction, with or without heptane. Therefore, either the surface was re-oxidized by residual oxygen, or the surface is not exceptionally reduced during this mild milling treatment.

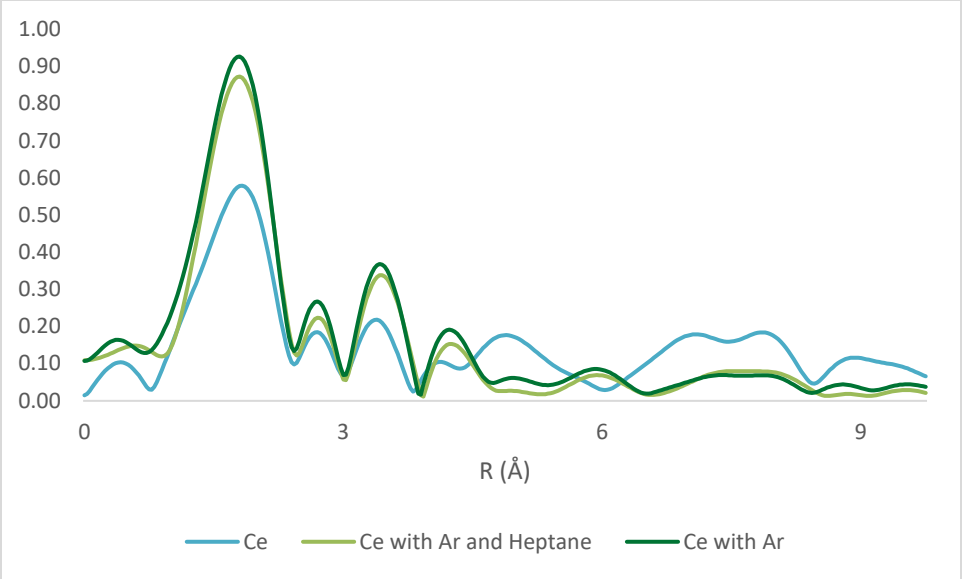

Figure 5.3. 5 Cerium R values

The milling seems to have interrupted the long-range order of the ceria fluorite lattice. The average radius between atoms shifted towards shorter lengths.

5.4 Discussion

During milling, no oxygenated products were observed with the mass spectrometer. This may have been due to the substantial survey of hydrocarbons which the machine was set to sample for; since heptane has so many carbons, there were many possible shorter carbon chains/oxygenated products, and this large quantity lengthened the sampling time considerably. Compounds may have been present, but not recorded, due to the long sampling time. It is also likely that there were no oxygenated products in the gas phase for the mass spectrometer to read.

The surface species on the catalyst were probed with infrared spectroscopy, and several bands in the C-O stretching region were observed. These bands were not present when heptane was physiosorbed onto the catalyst surface. Possible assignments are listed in the results section, but additional experiments, such as catalyst washing and GC analysis, should be performed to confirm or refute infrared assignments. To determine extent of reduction, three samples (fresh ceria zirconia, ceria zirconia milled in Ar, and ceria zirconia milled in Ar and heptane) were analyzed via XAS. The extent of reduction was minimal; the milling reduced long range order in the ceria cubic fluorite lattice structure

5.5 Conclusions

In conclusion, heptane seemed to be activated via ball milling with ceria zirconia, though greater study needs be performed to fully characterize this system. The surface moieties need to be irrefutably classified through multiple methods of characterization. The catalyst could be washed, and the liquid analyzed through gas chromatography to classify the organic species; the surface could also be analyzed with Raman spectroscopy to show structural information. After these experiments, reaction pathways can be tentatively assigned. The most pressing issue to address, after characterization, is the fact that the surface species need to be removed from the surface; this process would preferably remove the surface species in such a way that they enter the gas phase and are transported out of the reaction vessel, perhaps by feeding another molecule into the vessel.

Other hydrocarbons could also be activated in a similar manner. Methane has been shown to be activated in a ball mill with ceria to produce chloromethane [96]; perhaps

significant quantities of partial oxidation products, such as methanol, could be similarly formed.

CHAPTER 6. CONCLUSIONS AND RECOMMENDATIONS

6.1 Active Oxygen Species in Heterogeneous Catalyzed Oxidation Reactions

Active oxygen species are currently not well understood because there is no single analytical technique which can adequately describe all possible active surface species. If active oxygen species can be characterized, then catalyst surfaces can be tuned to produce selective oxygen species rather than unselective; therefore, understanding these oxygen species is important for the rational design of oxidation catalysts and research in this field should be pursued.

6.2 Study of Methane Partial Oxidation to Methanol with Modulation Excitation Spectroscopy

Methane partial oxidation to methanol over nickel- and copper-doped ceria zirconia catalysts was studied with Modulation Excitation Spectroscopy. Methane and oxygen concentrations were varied. Formates, precursors to carbon dioxide, often modulated with the alkoxy surface groups, the desired selective oxidation species. During oxygen modulation experiments over the bimetallic doped ceria zirconia, these two surface groups exhibited different phase shifts. This separation suggests that isothermal chemical looping may be an appropriate reaction engineering method to increase yield to methanol. Repeating the modulation experiments at other frequencies would provide additional kinetic information to determine appropriate cycling times for the chemical looping experiments.

6.3 Water Splitting via Mechanochemical Methods

Ceria was ball milled in the presence of water. Hydrogen was evolved, but this was likely due to the iron from the vessel and balls. These experiments should be repeated with a stronger vessel to determine if ceria can mechanically induce the water-splitting reaction.

6.4 Selective Oxidation of Heptane via Mechanochemical Methods

Heptane was activated when milled with ceria zirconia. The products were not rigorously characterized. However, these tests suggest that C-H bonds may be activated in by method; this method might be used to activate the strong methane C-H bond. Additional ball mill experiments are warranted.

APPENDIX A. MM400 BALL MILL SETUP

A Retsch Mixer Mill 400 was connected to a flow setup (see Figure A. 1 and Figure A. 2).

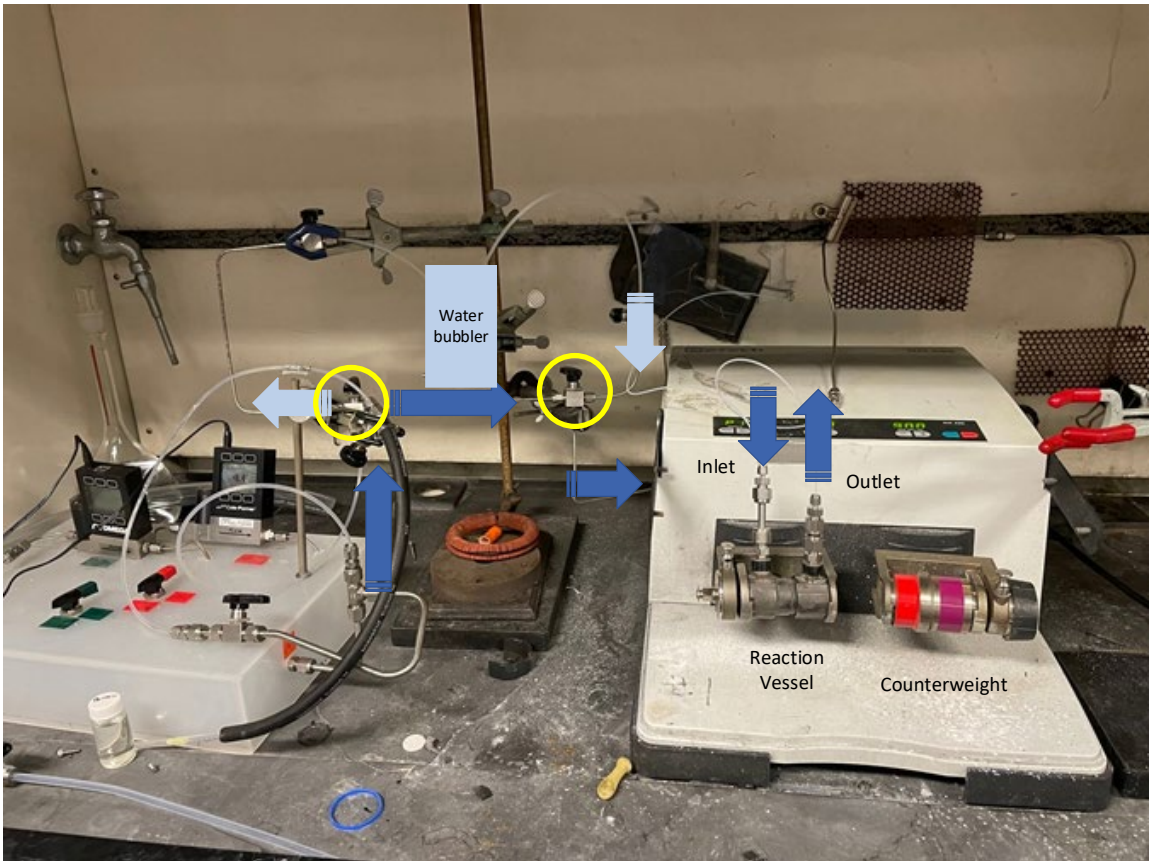

Figure A. 1 Image of the MM400 setup; flow path follows dark blue arrows unless circled valves are turned to admit water (light blue arrows)

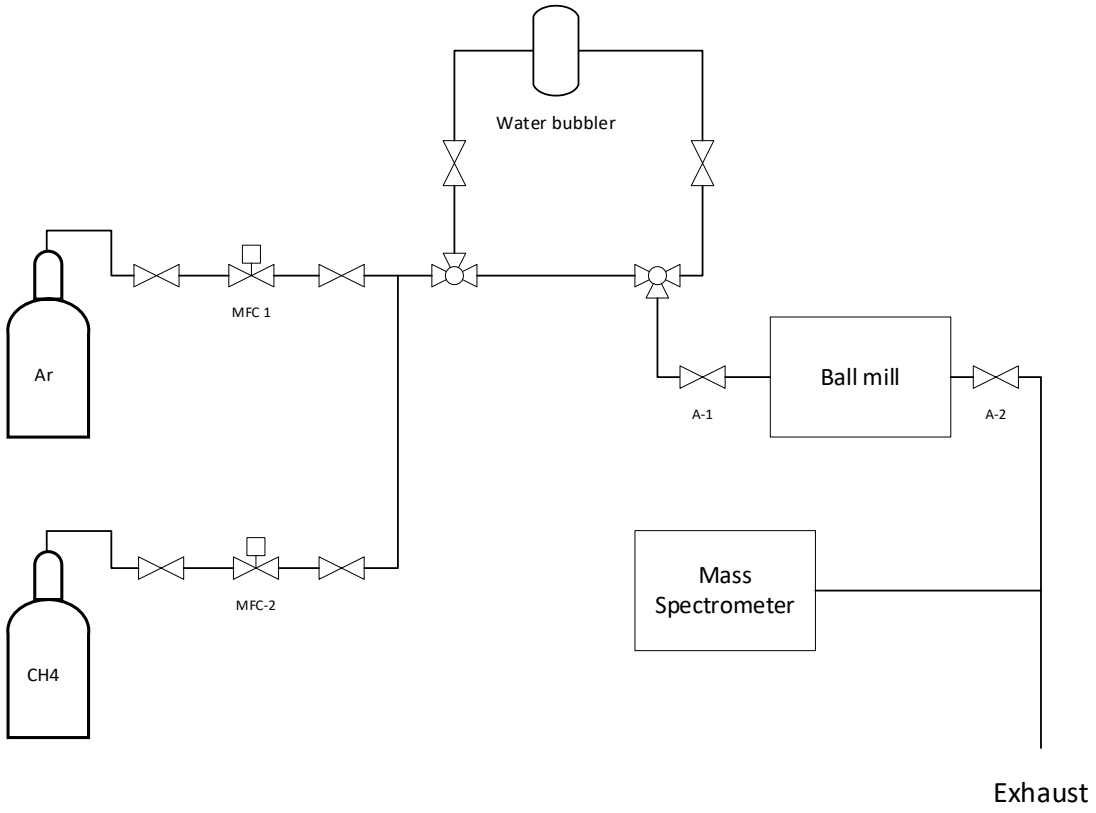

Figure A. 2 MM400 process flow diagram

A 25 mL stainless steel vessel, customized with two ports, one outlet and one inlet, was used for experiments. This vessel was connected to the flow setup via the listed parts in Figure A. 3.

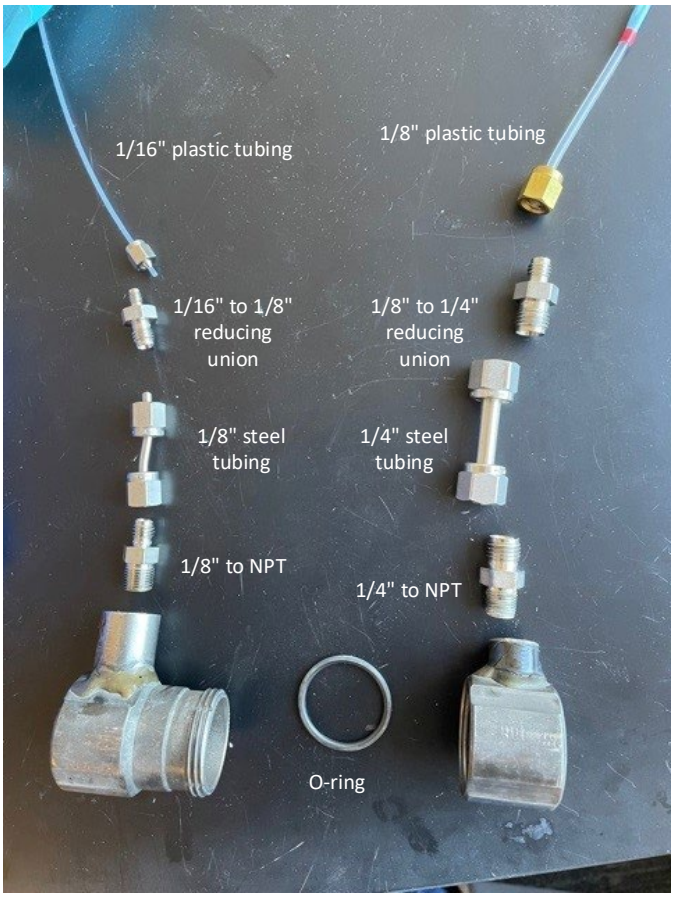

Figure A. 3 MM400 25 mL vessel connections

When analyzing oxidation state without exposing the powder to air, valves A-2 and A-1 were closed, the lines disconnected, and the vessel was transported to a glove box. It was unloaded under the Argon atmosphere inside of the glove box.

APPENDIX B. MM500 BALL MILL SETUP

A flow setup was installed around a Retsch Mixer Mill MM500, as can be seen in Figure B. 1 and Figure B. 2.

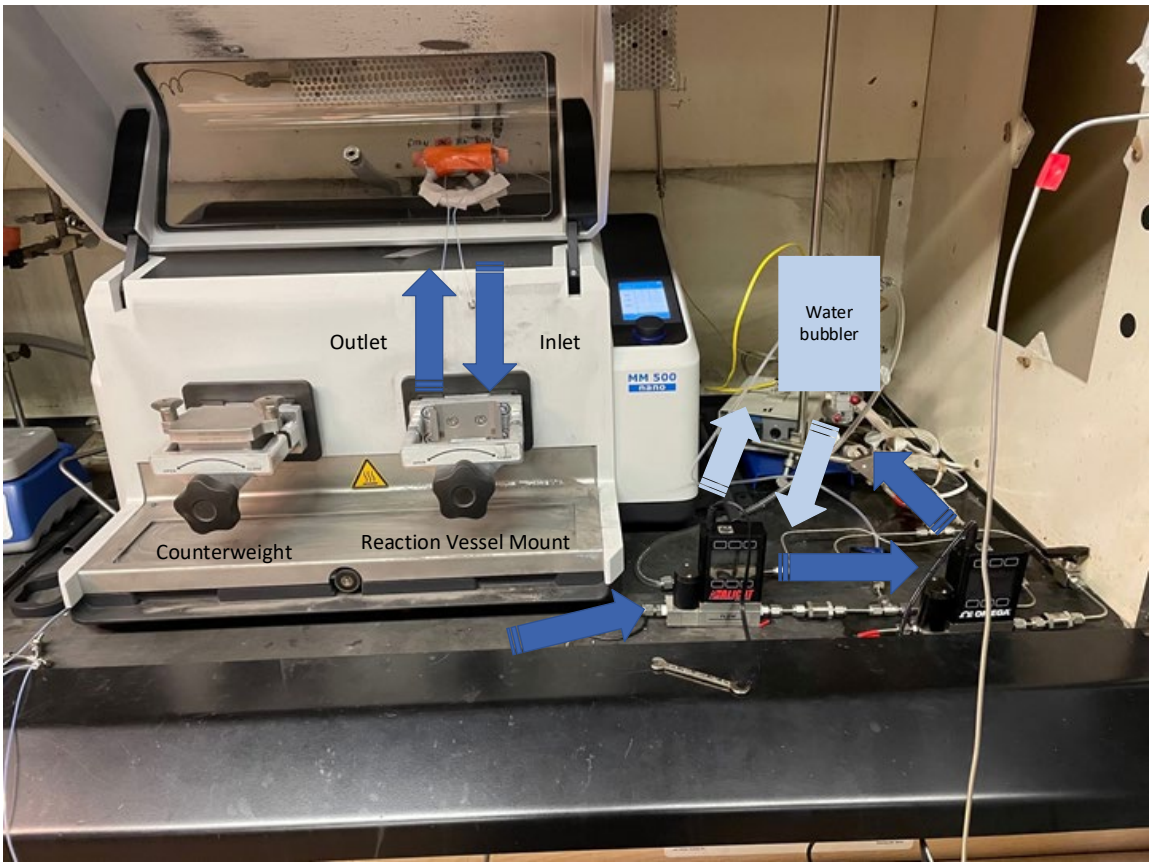

Figure B. 1 Image of the MM500 setup

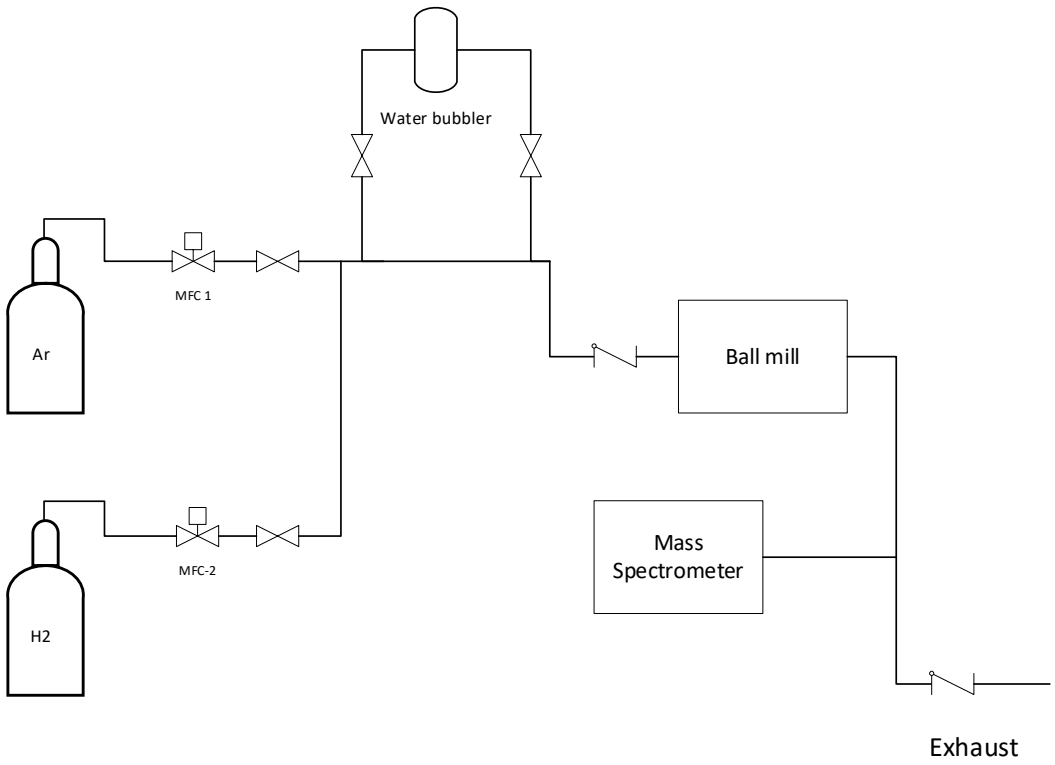

Figure B. 2 MM500 process flow diagram

A 125 mL stainless steel vessel, customized with inlet and outlet ports, was used for these experiments. Figure B. 3 shows the connections used to connect the vessel to the flow setup.

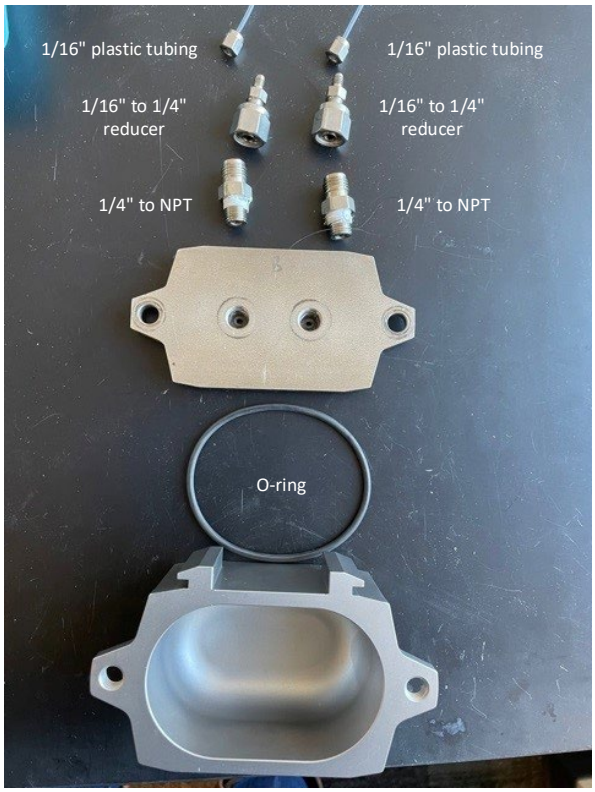

Figure B. 3 MM500 125 mL vessel connections

APPENDIX C. CERIA WATER SPLITTING SUPPORTING INFORMATION

The iron content (from PIXE results) is sufficient to explain both the hydrogen production and the TGA weight gain (Equations C1-C10).

Hydrogen production from iron in ceria:

Assuming a total mass of 10 g, and a mass fraction of 0.02216g Fe/g total (PIXE results from sample milled with water), there would be 0.2216 g Fe in the sample

$$3Fe + 4H_2O \rightarrow Fe_3O_4 + 4H_2 \quad \text{(C1)}$$

$$n_{Fe} = \frac{g_{Fe}}{MW_{Fe}} = \frac{0.2216}{55.845} = 0.003968\ mol\ Fe \quad \text{(C2)}$$

$$n_{H2} = \frac{n_{Fe}}{3} * 4 = 0.005291\ mol\ H_2 \quad \text{(C3)}$$

We can either consider 4 h or 2 h. 2 hours is the length of time that H_2 is observed; the total time, including the induction period, is 4 hours.

$$Min, vol.flow\ H_2 = \frac{n_{H2}}{4\ h * 60\ min/h} = 2.204x10^{-5}\ \text{mol/min} \quad \text{(C4)}$$

$$Max\ vol.flow\ H_2 = \frac{n_{H2}}{2\ h * 60\ min/h} = 4.409x10^{-5}\ \text{mol/min} \quad \text{(C5)}$$

This is sufficient to explain an observed flowrate of $3.5x10^{-5}$ mol/min

Observed TGA weight change from iron in ceria:

The δ_{TGA} was 0.034gO/g total. Assuming a mass fraction of 0.08285g Fe/ g total (PIXE results from sample which was milled in just Ar, without water) and a total mass of 10 g, there would be 0.8285 g Fe in the sample

$$3Fe + 4H_2O \rightarrow Fe_3O_4 + 4H_2 \tag{C6}$$

$$n_{Fe3O4} = \frac{g_{Fe}}{3MW_{Fe}} = \frac{0.8285}{3 * 55.845} = 0.004945\ mol\ Fe_3O_4 \tag{C7}$$

$$n_O = n_{Fe3O4} * 4 = 0.01978\ mol\ O \tag{C8}$$

$$m_O = n_O * MW_O = 0.01978 * 16 = 0.3165\ g\ O \tag{C9}$$

$$\delta = \frac{m_O}{m_{total}} = \frac{0.32}{10} = 0.032\ {}^{g\ O}/_{g\ total} \tag{C10}$$

The iron content can explain the weight gain observed.

APPENDIX D. MODULATION EXCITATION SPECTROSCOPY SUPPORTING INFORMATION

D.1 MES setup

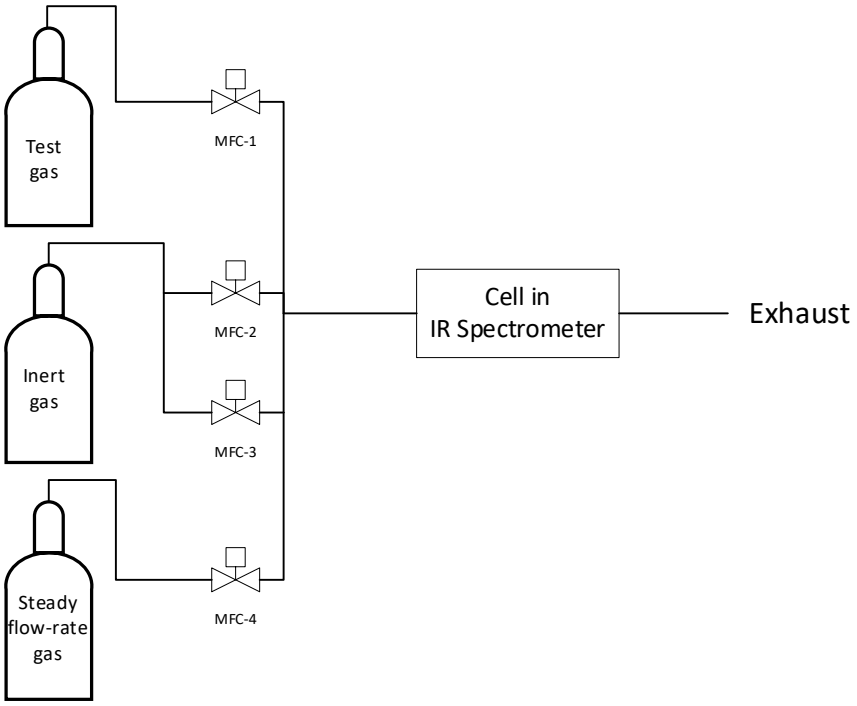

Figure D.1. 1 MES reaction set-up

All gasses (Ultra High Purity (UHP) Oxygen, UHP Nitrogen, research grade methane) were purchased from Airgas. Two mass flow controllers, MFC-1 and MFC-2, were controlled with a LabView program to deliver flowrates which modulated sinusoidally. For oxygen modulation experiments, oxygen was connected to MFC-1. Oxygen and nitrogen flowrates were modulated between 0 and 2 sccm, 180° out of phase with each other so that

the total flowrate remained constant (see Figure D.1. 2). Methane was fed at 10 sccm and nitrogen, from MFC-3, was fed at 38sccm. For methane modulation, methane was connected to MFC-1 and methane and nitrogen flowrates were modulated between 0 and 10 sccm (as in Figure D.1. 2 with the y-axis running from 0-10 instead of 0-2). Oxygen was fed at 2 sccm and nitrogen, via MFC-3, was fed at 38sccm.

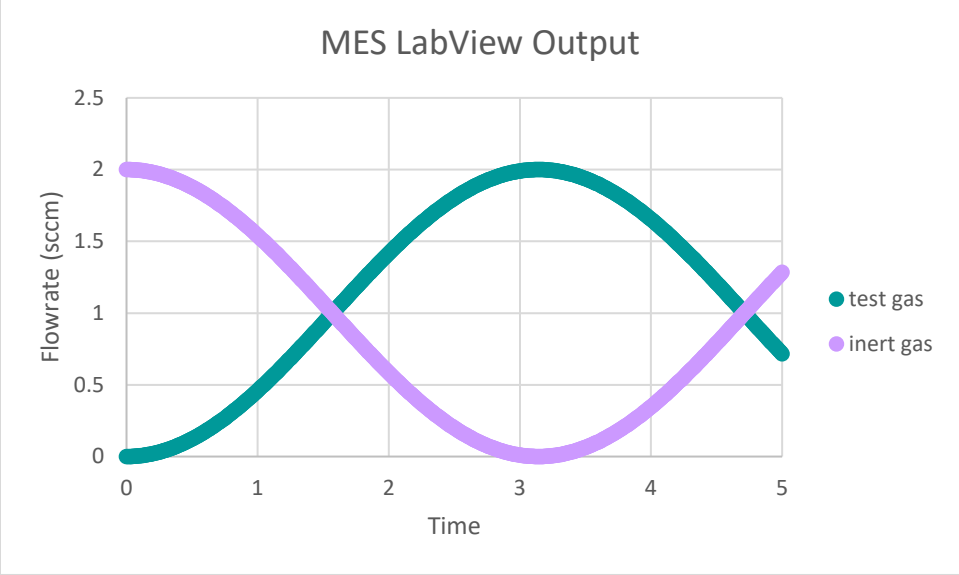

Figure D.1. 2 MES flowrates as controlled by LabVIEW; the test gas and the inert gas flowrates follow two sine waves, 180° out of sync with each other, to keep the total flowrate constant

The period used for the oxygen modulation experiments was 600 seconds. Spectra were collected every 12 seconds, with 16 scans at a resolution of 4 cm-1, for 180 minutes. For methane modulation experiments, the period was 1800 seconds. Spectra were collected every 30 seconds, with 32 scans at a resolution of 4 cm-1, for 240 minutes.

D.2 Synopsis of MES mathematical formulation

Detailed descriptions of the theoretical underpinnings of this method may be found in the reviews by Baurecht and Fringeli [45] and Srinivsan et al. [47]. For these experiments, the stimulus (concentration) is modulated sinusoidally. Any periodic function can be described as a Fourier series

$$f(t) = a_0 + \sum_{k=1}^{\infty} [a_k \cos(k\omega t) + b_k \sin(k\omega t)] \tag{D1}$$

Where $\omega = 2\pi f = \frac{2\pi}{T}$ and k is the frequency multiplier and a_k and b_k are Fourier coefficients ($a_0 = \frac{1}{T}\int_0^T f(t)dt$; $a_k = \frac{2}{T}\int_0^T f(t)\cos(k\omega t)dt$; $b_k = \frac{2}{T}\int_0^T f(t)\sin(k\omega t)dt$). The goal of these experiments is to ascertain which surface species modulate in sync with the applied concentration modulation and which do not; therefore, an additional phase angle must be expressed in the equation. a_k and b_k, the Fourier coefficients, can also be expressed in polar coordinates with amplitude c_k and phase angle φ_k, e.g. $a_k = c_k sin\varphi_k$ and $b_k = c_k cos\varphi_k$. The Fourier series (D1) can be written as

$$\begin{aligned} f(t) &= a_0 + \sum_{k=1}^{\infty} [c_k sin\varphi_k \cos(k\omega t) + c_k cos\varphi_k \sin(k\omega t)] \\ &= a_0 + \sum_{k=1}^{\infty} [c_k sin(k\omega t + \varphi_k)] \end{aligned} \tag{D2}$$

Where amplitude and phase lag are given by: $c_k = \sqrt{a_k^2 + b_k^2}$, $sin\varphi_k = \frac{a_k}{c_k}$, $\cos\varphi_k = \frac{b_k}{c_k}$. When this equation is used to describe absorbance (what the spectrometer records) for N species, the following series results:

$$A(\tilde{\nu}, t) = \sum_{i=1}^{N} A_i\,(\tilde{\nu}, t)$$

$$= \sum_{i=1}^{N} A_{i,0}\,(\tilde{\nu}) \tag{D3}$$

$$+ \sum_{i=1}^{N} \sum_{k=1}^{\infty} A_{i,k}^{90^\circ}(\tilde{\nu}) \cos(k\omega t) + A_{i,k}^{0^\circ}(\tilde{\nu}) \sin(k\omega t)$$

Equation (D3) is comprised of a stationary and modulating part. $A_{i,0}(\tilde{\nu})$ is the mean absorbance per period (stationary); the $A_{i,k}^{90^\circ}(\tilde{\nu})$ term is associated with the cosine, 90° out of phase, components and the $A_{i,k}^{0^\circ}(\tilde{\nu})$ is associated with the 0°, in phase components (The remaining equations in this section will be simplified to only relate to one species, e.g. equation (D3) represented as a sine series becomes equation (D4)).

$$A(\tilde{\nu}, t) = A_0(\tilde{\nu}) + \sum_{k=1}^{\infty} A_k(\tilde{\nu}) \sin\,[k\omega t + \varphi_k(\tilde{\nu})] \tag{D4}$$

$A_k(\tilde{\nu})$ denotes the average amplitude, and it is composed of absorbances $A_{ik}(\tilde{\nu})$ of all species X_i absorbing at wavenumber $\tilde{\nu}$. Each of these components has a distinct phase lag $\varphi_{ik}(\tilde{\nu})$. Phase sensitive detection (PSD) involves multiplying $A(\tilde{\nu}, t)$ by $\sin\,(k\omega t +$

φ_k^{PSD}) and then normalizing the integral over the period T. This introduces a new parameter, the phase angle φ_k^{PSD}, i.e.

$$A_k^{\varphi_k^{PSD}}(\tilde{\nu}) = \frac{2}{T}\int_0^T A(\tilde{\nu}, t)\sin(k\omega t + \varphi_k^{PSD})\,dt \tag{D5}$$

$A_k^{\varphi_k^{PSD}}(\tilde{\nu})$ is the phase-resolved spectrum associated with the frequency $k\omega$. For the special cases $\varphi_k^{PSD} = 0°$ and $\varphi_k^{PSD} = 90°$, $A_k^{\varphi_k^{PSD}}(\tilde{\nu})$ is equivalent to the in-phase and out of phase components of equation (D3). φ_k^{PSD} can be written as a linear combination of the in-phase and out of phase components and thus, phase shifts can be extracted from the time-dependent overall absorbance.

REFERENCES

[1] F. Cavani, Catalytic selective oxidation: The forefront in the challenge for a more sustainable chemical industry, Catal. Today. 157 (2010) 8–15. https://doi.org/10.1016/j.cattod.2010.02.072.

[2] F. Cavani, J.H. Teles, Sustainability in catalytic oxidation: An alternative approach or a structural evolution?, ChemSusChem. 2 (2009) 508–534. https://doi.org/10.1002/cssc.200900020.

[3] C.M. Friend, B. Xu, Heterogeneous catalysis: A central science for a sustainable future, Acc. Chem. Res. 50 (2017) 517–521. https://doi.org/10.1021/acs.accounts.6b00510.

[4] U.S. Energy Information Administration, Natural Gas Gross Withdrawls, (2021). https://www.eia.gov/dnav/ng/ng_prod_sum_a_EPG0_VGV_mmcf_a.htm.

[5] R.B. Jackson, E.I. Solomon, J.G. Canadell, M. Cargnello, C.B. Field, Methane removal and atmospheric restoration, Nat. Sustain. 2 (2019) 436–438. https://doi.org/10.1038/s41893-019-0299-x.

[6] A.I. Olivos-Suarez, À. Szécsényi, E.J.M. Hensen, J. Ruiz-Martinez, E.A. Pidko, J. Gascon, Strategies for the Direct Catalytic Valorization of Methane Using Heterogeneous Catalysis: Challenges and Opportunities, ACS Catal. 6 (2016) 2965–2981. https://doi.org/10.1021/acscatal.6b00428.

[7] A.A. Latimer, A. Kakekhani, A.R. Kulkarni, J.K. Nørskov, Direct Methane to Methanol: The Selectivity-Conversion Limit and Design Strategies, ACS Catal. 8 (2018) 6894–6907. https://doi.org/10.1021/acscatal.8b00220.

[8] Z. Wei, J. Sun, Y. Li, A.K. Datye, Y. Wang, Bimetallic catalysts for hydrogen generation, Chem. Soc. Rev. 41 (2012) 7994–8008. https://doi.org/10.1039/c2cs35201j.

[9] A. Le Gal, S. Abanades, N. Bion, T. Le Mercier, V. Harlé, Reactivity of doped ceria-based mixed oxides for solar thermochemical hydrogen generation via two-step water-splitting cycles, Energy and Fuels. 27 (2013) 6068–6078. https://doi.org/10.1021/ef4014373.

[10] S. Abanades, G. Flamant, Thermochemical hydrogen production from a two-step solar-driven water-splitting cycle based on cerium oxides, Sol. Energy. 80 (2006) 1611–1623. https://doi.org/10.1016/j.solener.2005.12.005.

[11] A. Haeussler, S. Abanades, J. Jouannaux, M. Drobek, A. Ayral, A. Julbe, Recent progress on ceria doping and shaping strategies for solar thermochemical water and CO2 splitting cycles, AIMS Mater. Sci. 6 (2019) 657–684. https://doi.org/10.3934/MATERSCI.2019.5.657.

[12] F. Delogu, Hydrogen generation by mechanochemical reaction of quartz powders in water, Int. J. Hydrogen Energy. 36 (2011) 15145–15152.

[13] Y. Sawama, M. Niikawa, Y. Yabe, R. Goto, T. Kawajiri, T. Marumoto, T. Takahashi, M. Itoh, Y. Kimura, Y. Sasai, Y. Yamauchi, S.I. Kondo, M. Kuzuya, Y. Monguchi, H. Sajiki, Stainless-steel-mediated quantitative hydrogen generation from water under ball milling conditions, ACS Sustain. Chem. Eng. 3 (2015) 683–689. https://doi.org/10.1021/sc5008434.

[14] Y. Sawama, T. Kawajiri, M. Niikawa, R. Goto, Y. Yabe, T. Takahashi, T. Marumoto, M. Itoh, Y. Kimura, Y. Monguchi, S.I. Kondo, H. Sajiki, Stainless-Steel Ball-Milling Method for Hydro-/Deutero-genation using H2O/D2O as a Hydrogen/Deuterium Source, ChemSusChem. 8 (2015) 3773–3776. https://doi.org/10.1002/cssc.201501019.

[15] Y. Sawama, N. Yasukawa, K. Ban, R. Goto, M. Niikawa, Y. Monguchi, M. Itoh, H. Sajiki, Stainless Steel-Mediated Hydrogen Generation from Alkanes and Diethyl Ether and Its Application for Arene Reduction, Org. Lett. 20 (2018) 2892–2896. https://doi.org/10.1021/acs.orglett.8b00931.

[16] D. Chen, S. Ni, Z. Chen, Synthesis of Fe3O4 nanoparticles by wet milling iron powder in a planetary ball mill, China Particuology. 5 (2007) 357–358. https://doi.org/10.1016/j.cpart.2007.05.005.

[17] S.S. Razavi-Tousi, J.A. Szpunar, Effect of structural evolution of aluminum powder during ball milling on hydrogen generation in aluminum-water reaction, Int. J. Hydrogen Energy. 38 (2013) 795–806. https://doi.org/10.1016/j.ijhydene.2012.10.106.

[18] O.C. Williams, C. Sievers, Active oxygen species in heterogeneously catalyzed oxidation reactions, Appl. Catal. A, Gen. 614 (2021) 118057. https://doi.org/10.1016/j.apcata.2021.118057.

[19] J.P. Kehrer, J.D. Robertson, C. V. Smith, Free Radicals and Reactive Oxygen Species, Compr. Toxicol. Second Ed. 1–14 (2010) 277–307. https://doi.org/10.1016/B978-0-08-046884-6.00114-7.

[20] X. Liu, Y. Ryabenkova, M. Conte, Catalytic oxygen activation versus autoxidation for industrial applications: A physicochemical approach, Phys. Chem. Chem. Phys. 17 (2015) 715–731. https://doi.org/10.1039/c4cp03568b.

[21] J. Nordberg, E.S.J. Arnér, Reactive oxygen species, antioxidants, and the mammalian thioredoxin system, Free Radic. Biol. Med. 31 (2001) 1287–1312. https://doi.org/10.1016/S0891-5849(01)00724-9.

[22] S. Duanghathaipornsuk, E.J. Farrell, A.C. Alba-Rubio, P. Zelenay, D.S. Kim, Detection Technologies for Reactive Oxygen Species: Fluorescence and Electrochemical Methods and Their Applications, Biosensors. 11 (2021). https://doi.org/10.3390/bios11020030.

[23] M. Ravi, V.L. Sushkevich, A.J. Knorpp, M.A. Newton, D. Palagin, A.B. Pinar, M. Ranocchiari, J.A. van Bokhoven, Misconceptions and challenges in methane-to-methanol over transition-metal-exchanged zeolites, Nat. Catal. 2 (2019) 485–494. https://doi.org/10.1038/s41929-019-0273-z.

[24] U.S. Energy Information Administration, Annual Report of Domestic Oil and Gas Reserves, 2019. https://www.eia.gov/naturalgas/crudeoilreserves/.

[25] M. Ravi, M. Ranocchiari, J.A. van Bokhoven, The Direct Catalytic Oxidation of Methane to Methanol—A Critical Assessment, Angew. Chemie - Int. Ed. 56 (2017) 16464–16483. https://doi.org/10.1002/anie.201702550.

[26] H.F. Rase, Handbook of Commercial Catalysts: heterogeneous catalysts, CRC Press LLC, Boca Raton, 2000.

[27] D.W. Choi, R.C. Kunz, E.S. Boyd, J.D. Semrau, W.E. Antholine, J.I. Han, J.A. Zahn, J.M. Boyd, A.M. De la Mora, A.A. DiSpirito, The membrane-associated methane monooxygenase (pMMO) and pMMO-NADH:Quinone oxidoreductase complex from Methylococcus capsulatus bath, J. Bacteriol. 185 (2003) 5755–5764. https://doi.org/10.1128/JB.185.19.5755-5764.2003.

[28] J. Zang, J.D. Lipscomb, Role of the C-Terminal Region of the B Component of Methylosinus trichosporium OB3b Methane Monooxygenase in the Regulation of

Oxygen Activation, Biochemistry. 45 (2006) 1459–1469.

[29] C. Hammond, S. Conrad, I. Hermans, Oxidative methane upgrading, ChemSusChem. 5 (2012) 1668–1686. https://doi.org/10.1002/cssc.201200299.

[30] M.H. Groothaert, P.J. Smeets, B.F. Sels, P.A. Jacobs, R.A. Schoonheydt, Selective oxidation of methane by the bis(μ-oxo)dicopper core stabilized on ZSM-5 and mordenite zeolites, J. Am. Chem. Soc. 127 (2005) 1394–1395. https://doi.org/10.1021/ja047158u.

[31] J.S. Woertink, P.J. Smeets, M.H. Groothaert, M.A. Vance, B.F. Sels, R.A. Schoonheydt, E.I. Solomon, A [Cu2O]2+ core in Cu-ZSM-5, the active site in the oxidation of methane to methanol, Proc. Natl. Acad. Sci. U. S. A. 106 (2009) 18908–18913. https://doi.org/10.1073/pnas.0910461106.

[32] D. Radu, P. Glatze, A. Gloter, O. Stephan, B.M. Weckhuysen, F.M.F. De Groot, Geometric and electronic structure of α-oxygen sites in Mn-ZSM-5 zeolites, J. Phys. Chem. C. 112 (2008) 12409–12416. https://doi.org/10.1021/jp802915k.

[33] P. Tomkins, M. Ranocchiari, J.A. Van Bokhoven, Direct Conversion of Methane to Methanol under Mild Conditions over Cu-Zeolites and beyond, Acc. Chem. Res. 50 (2017) 418–425. https://doi.org/10.1021/acs.accounts.6b00534.

[34] D.K. Pappas, A. Martini, M. Dyballa, K. Kvande, S. Teketel, K.A. Lomachenko, R. Baran, P. Glatzel, B. Arstad, G. Berlier, C. Lamberti, S. Bordiga, U. Olsbye, S. Svelle, P. Beato, E. Borfecchia, The Nuclearity of the Active Site for Methane to Methanol Conversion in Cu-Mordenite: A Quantitative Assessment, J. Am. Chem. Soc. 140 (2018) 15270–15278. https://doi.org/10.1021/jacs.8b08071.

[35] G. Wang, L. Huang, W. Chen, J. Zhou, A. Zheng, Rationally designing mixed Cu-(μ-O)-M (M = Cu, Ag, Zn, Au) centers over zeolite materials with high catalytic activity towards methane activation, Phys. Chem. Chem. Phys. 20 (2018) 26522–26531. https://doi.org/10.1039/c8cp04872j.

[36] N. Luo, K. Ouyang, F. Cao, T. Xiao, Hydrogen generation from liquid reforming of glycerin over Ni-Co bimetallic catalyst, Biomass and Bioenergy. 34 (2010) 489–495. https://doi.org/10.1016/j.biombioe.2009.12.013.

[37] P. Tomkins, A. Mansouri, V. L. Sushkevich, L.I. Van der Wal, S.E. Bozbag, F. Krumeich, M. Ranocchiari, J.A. Van Bokhoven, Increasing the activity of copper

exchanged mordenite in the direct isothermal conversion of methane to methanol by Pt and Pd doping, Chem. Sci. 10 (2019) 167–171. https://doi.org/10.1039/C8SC02795A.

[38] P.G. Lustemberg, R.M. Palomino, R.A. Gutiérrez, D.C. Grinter, M. Vorokhta, Z. Liu, P.J. Ramírez, V. Matolín, M.V. Ganduglia-Pirovano, S.D. Senanayake, J.A. Rodriguez, Direct Conversion of Methane to Methanol on Ni-Ceria Surfaces: Metal-Support Interactions and Water-Enabled Catalytic Conversion by Site Blocking, J. Am. Chem. Soc. 140 (2018) 7681–7687. https://doi.org/10.1021/jacs.8b03809.

[39] S.A. Larrondo, A. Kodjaian, I. Fábregas, M.G. Zimicz, D.G. Lamas, B.E. Walsöe de Reca, N.E. Amadeo, Methane partial oxidation using Ni/Ce0.9Zr0.1O2 catalysts, Int. J. Hydrogen Energy. 33 (2008) 3607–3613. https://doi.org/10.1016/j.ijhydene.2008.04.025.

[40] P. Pue-On, V. Meeyoo, T. Rirksombooon, Methane partial oxidation over NiO-MgO/Ce0.75Zr0.25O2 catalysts, Front. Chem. Sci. Eng. 7 (2013) 289–296. https://doi.org/10.1007/s11705-013-1345-2.

[41] Y. Lyu, J.N. Jocz, R. Xu, O.C. Williams, C. Sievers, Selective Oxidation of Methane to Methanol over Ceria-Zirconia Supported Mono and Bimetallic Transition Metal Oxide Catalysts, ChemCatChem. 13 (2021) 2832–2842. https://doi.org/10.1002/cctc.202100268.

[42] Y. Lyu, R. Xu, O. Williams, Z. Wang, C. Sievers, Reaction paths of methane activation and oxidation of surface intermediates over NiO on Ceria-Zirconia catalysts studied by In-situ FTIR spectroscopy, J. Catal. 404 (2021) 334–347. https://doi.org/10.1016/j.jcat.2021.10.004.

[43] M.E. Witzke, A. Almithn, C.L. Conrad, M.D. Triezenberg, D.D. Hibbitts, D.W. Flaherty, In Situ Methods for Identifying Reactive Surface Intermediates during Hydrogenolysis Reactions: C-O Bond Cleavage on Nanoparticles of Nickel and Nickel Phosphides, J. Am. Chem. Soc. 141 (2019) 16671–16684. https://doi.org/10.1021/jacs.9b06112.

[44] N. Maeda, F. Meemken, K. Hungerbühler, A. Baiker, Spectroscopic detection of active species on catalytic surfaces: Steady-state versus transient method, Chimia (Aarau). 66 (2012) 664–667. https://doi.org/10.2533/chimia.2012.664.

[45] D. Baurecht, U.P. Fringeli, Quantitative modulated excitation Fourier transform infrared spectroscopy, Rev. Sci. Instrum. 72 (2001) 3782–3792.

https://doi.org/10.1063/1.1400152.

[46] A. Urakawa, T. Bürgi, A. Baiker, Sensitivity enhancement and dynamic behavior analysis by modulation excitation spectroscopy: Principle and application in heterogeneous catalysis, Chem. Eng. Sci. 63 (2008) 4902–4909. https://doi.org/10.1016/j.ces.2007.06.009.

[47] P.D. Srinivasan, B.S. Patil, H. Zhu, J.J. Bravo-Suárez, Application of modulation excitation-phase sensitive detection-DRIFTS for: In situ /operando characterization of heterogeneous catalysts, React. Chem. Eng. 4 (2019) 862–883. https://doi.org/10.1039/c9re00011a.

[48] G. Armelles, M.I. Alonso, P. Castrillo, P.S. Domínguez, Modulation excitation spectroscopy: A method to determine the symmetry of electronic states, Appl. Phys. Lett. 60 (1992) 3277–3279. https://doi.org/10.1063/1.106718.

[49] Y. Lyu, J. Jocz, R. Xu, E. Stavitski, C. Sievers, Nickel Speciation and Methane Dry Reforming Performance of Ni/CexZr1- xO2Prepared by Different Synthesis Methods, ACS Catal. 10 (2020) 11235–11252. https://doi.org/10.1021/acscatal.0c02426.

[50] S.M. Schimming, G.S. Foo, O.D. Lamont, A.K. Rogers, M.M. Yung, A.D. D'Amico, C. Sievers, Kinetics of hydrogen activation on ceria-zirconia, J. Catal. 329 (2015) 335–347. https://doi.org/10.1016/j.jcat.2015.05.027.

[51] S. Brunauer, P.H. Emmett, E. Teller, Adsorption of Gases in Multimolecular Layers, J. Am. Chem. Soc. 60 (1938) 309–319.

[52] E.P. Barrett, L.G. Joyner, P.P. Halenda, The Determination of Pore Volume and Area Distributions in Porous Substances., J. Am. Chem. Soc. 73 (1951) 373–380.

[53] J. Wang, V.F. Kispersky, W. Nicholas Delgass, F.H. Ribeiro, Determination of the Au active site and surface active species via operando transmission FTIR and isotopic transient experiments on 2.3 wt.% Au/TiO 2 for the WGS reaction, J. Catal. 289 (2012) 171–178. https://doi.org/10.1016/j.jcat.2012.02.008.

[54] M.I. Zaki, G.A.M. Hussein, S.A.A. Mansour, H.A. El-Ammawy, Adsorption and surface reactions of pyridine on pure and doped ceria catalysts as studied by infrared spectroscopy, J. Mol. Catal. 51 (1989) 209–220. https://doi.org/10.1016/0304-5102(89)80101-4.

[55] N.B. Colthup, L.H. Daly, S.E. Wiberley, Introduction to Infrared and Raman Spectroscopy, 3rd ed., Academic Press, New York, 1990.

[56] G.N. Vayssilov, M. Mihaylov, P.S. Petkov, K.I. Hadjiivanov, K.M. Neyman, Reassignment of the vibrational spectra of carbonates, formates, and related surface species on ceria: A combined density functional and infrared spectroscopy investigation, J. Phys. Chem. C. 115 (2011) 23435–23454. https://doi.org/10.1021/jp208050a.

[57] C. Li, Y. Sakata, T. Arai, K. Domen, K. Maruya, Adsorption of Carbon Monoxide and Carbon Dioxide on Cerium Oxide studied by Fourier- transform Infrared Spectroscopy, J. Chem. Soc., Faraday Trans. 85 (1989) 1451–1461.

[58] T. Tabakova, F. Boccuzzi, M. Manzoli, D. Andreeva, FTIR study of low-temperature water-gas shift reaction on gold/ceria catalyst, Appl. Catal. A Gen. 252 (2003) 385–397. https://doi.org/10.1016/S0926-860X(03)00493-9.

[59] M. Marwood, R. Doepper, A. Renken, In-situ surface and gas phase analysis for kinetic studies under transient conditions The catalytic hydrogenation of CO2, Appl. Catal. A Gen. 151 (1997) 223–246. https://doi.org/10.1007/978-94-007-0053-66.

[60] H. Miyata, T. Ohno, F. Hatayama, FTIR studies of the interaction of aromatic hydrocarbons with vanadium oxide layered on ZrO2 and TiO2, J. Chem. Soc. Faraday Trans. 91 (1995) 3505–3510. https://doi.org/10.1039/FT9959103505.

[61] H. Gulley-Stahl, P.A. Hogan, W.L. Schmidt, S.J. Wall, A. Buhrlage, H.A. Bullen, Response to “comment on 'surface complexation of catechol to metal oxides: An ATR-FTIR, adsorption, and dissolution study,” Environ. Sci. Technol. 44 (2010) 6519. https://doi.org/10.1021/es102327j.

[62] X. Tang, Y. Xu, W. Shen, Promoting effect of copper on the catalytic activity of MnOx-CeO2 mixed oxide for complete oxidation of benzene, Chem. Eng. J. 144 (2008) 175–180. https://doi.org/10.1016/j.cej.2008.01.016.

[63] W.-C. Wu, L.-F. Liao, C.-F. Lien, J.-L. Lin, FTIR study of adsorption, thermal reactions and photochemistry of benzene on powdered TiO2, Phys. Chem. Chem. Phys. 3 (2001) 4456–4461. https://doi.org/10.1021/jp004285d.

[64] F.C. Meunier, D. Reid, A. Goguet, S. Shekhtman, C. Hardacre, R. Burch, W. Deng, M. Flytzani-Stephanopoulos, Quantitative analysis of the reactivity of formate

species seen by DRIFTS over a Au/Ce(La)O2 water-gas shift catalyst: First unambiguous evidence of the minority role of formates as reaction intermediates, J. Catal. 247 (2007) 277–287. https://doi.org/10.1016/j.jcat.2007.02.013.

[65] F.C. Meunier, D. Tibiletti, A. Goguet, D. Reid, R. Burch, On the reactivity of carbonate species on a Pt/CeO2 catalyst under various reaction atmospheres: Application of the isotopic exchange technique, Appl. Catal. A Gen. 289 (2005) 104–112. https://doi.org/10.1016/j.apcata.2005.04.018.

[66] G. Socrates, Infrared and Raman characteristic group frequencies. Tables and charts, 2001. http://doi.wiley.com/10.1002/jrs.1238.

[67] L.J. Burcham, L.E. Briand, I.E. Wachs, Quantification of active sites for the determination of methanol oxidation turn-over frequencies using methanol chemisorption and in situ infrared techniques. 1 Supported metal oxide catalysts, Langmuir. 17 (2001) 6164–6174. https://doi.org/10.1021/la010010t.

[68] R. Singuru, J. Lee, K. Dhanalaxmi, B.M. Reddy, K. An, J. Mondal, Design of Efficient Noble Metal Free Copper-Promoted Nickel-Ceria-Zirconia Nanocatalyst for Bio-Fuel Upgrading, Chem. Sel. 3 (2018) 6174–6185.

[69] S. Ghosh, S. Hariharan, A.K. Tiwari, Water Adsorption and Dissociation on Copper/Nickel Bimetallic Surface Alloys: Effect of Surface Temperature on Reactivity, J. Phys. Chem. C. 121 (2017) 16351–16365. https://doi.org/10.1021/acs.jpcc.7b04637.

[70] J.P. Lange, V.L. Sushkevich, A.J. Knorpp, J.A. Van Bokhoven, Methane-to-Methanol via Chemical Looping: Economic Potential and Guidance for Future Research, Ind. Eng. Chem. Res. 58 (2019) 8674–8680. https://doi.org/10.1021/acs.iecr.9b01407.

[71] V.L. Sushkevich, D. Palagin, M. Ranocchiari, J.A. van Bokhoven, synthesis of methanol, Science (80-.). 356 (2017) 523–527.

[72] S.E. Bozbag, P. Sot, M. Nachtegaal, M. Ranocchiari, J.A. Van Bokhoven, C. Mesters, Direct Stepwise Oxidation of Methane to Methanol over Cu-SiO2, ACS Catal. 8 (2018) 5721–5731. https://doi.org/10.1021/acscatal.8b01021.

[73] W.D. Callister, D.G. Rethwisch, Materials Science and Engineering: An introduction, John Wiley & Sons, 2014.

[74] S. Kwon, M. Fan, H.F.M. DaCosta, A.G. Russell, K.A. Berchtold, M.K. Dubey, CO2 Sorption, Elsevier Inc., 2011. https://doi.org/10.1016/b978-0-8155-2049-8.10010-5.

[75] P. Tomkins, A. Mansouri, S.E. Bozbag, F. Krumeich, M.B. Park, E.M.C. Alayon, M. Ranocchiari, J.A. Vanbokhoven, Isothermal Cyclic Conversion of Methane into Methanol over Copper-Exchanged Zeolite at Low Temperature, Angew. Chemie - Int. Ed. 55 (2016) 5467–5471. https://doi.org/10.1002/anie.201511065.

[76] V.L. Sushkevich, J.A. Van Bokhoven, Methane-to-Methanol: Activity Descriptors in Copper-Exchanged Zeolites for the Rational Design of Materials, ACS Catal. 9 (2019) 6293–6304. https://doi.org/10.1021/acscatal.9b01534.

[77] J. Zhu, V.L. Sushkevich, A.J. Knorpp, M.A. Newton, S.C.M. Mizuno, T. Wakihara, T. Okubo, Z. Liu, J.A. Van Bokhoven, Cu-Erionite Zeolite Achieves High Yield in Direct Oxidation of Methane to Methanol by Isothermal Chemical Looping, Chem. Mater. 32 (2020) 1448–1453. https://doi.org/10.1021/acs.chemmater.9b04223.

[78] S. Fouladvand, M. Skoglundh, P.A. Carlsson, A transient in situ infrared spectroscopy study on methane oxidation over supported Pt catalysts, Catal. Sci. Technol. 4 (2014) 3463–3473. https://doi.org/10.1039/c4cy00486h.

[79] S.L. James, C.J. Adams, C. Bolm, D. Braga, P. Collier, T. Frišcic, F. Grepioni, K.D.M. Harris, G. Hyett, W. Jones, A. Krebs, J. Mack, L. Maini, A.G. Orpen, I.P. Parkin, W.C. Shearouse, J.W. Steed, D.C. Waddell, Mechanochemistry: opportunities for new and cleaner synthesis, Chem. Soc. Rev. 41 (2012) 413–447. https://doi.org/10.1039/c1cs15171a.

[80] E. Boldyreva, Mechanochemistry of inorganic and organic systems: What is similar, what is different?, Chem. Soc. Rev. 42 (2013) 7719–7738. https://doi.org/10.1039/c3cs60052a.

[81] V. V. Molchanov, R.A. Buyanov, Mechanochemistry of catalysts, Russ. Chem. Rev. 69 (2000) 490–493. https://doi.org/10.1070/rc2000v069n05abeh000555.

[82] J.G. Hernandez, C−H Bond Functionalization by Mechanochemistry, Chem. - A Eur. J. 23 (2017) 17157–17165.

[83] C. Bolm, J.G. Hernández, Mechanochemistry of gaseous reactantants, Angew. Chemie. 131 (2019) 3320–3335. https://doi.org/10.1002/ange.201810902.

[84] A.W. Tricker, G. Samaras, K.L. Hebisch, M.J. Realff, C. Sievers, Hot spot generation, reactivity, and decay in mechanochemical reactors, Chem. Eng. J. 382 (2020) 122954. https://doi.org/10.1016/j.cej.2019.122954.

[85] R. Eckert, M. Felderhoff, F. Schüth, Preferential Carbon Monoxide Oxidation over Copper-Based Catalysts under In Situ Ball Milling, Angew. Chemie. 129 (2017) 2485–2488. https://doi.org/10.1002/ange.201610501.

[86] R. Schmidt, H. Martin Scholze, A. Stolle, Temperature progression in a mixer ball mill, Int. J. Ind. Chem. 7 (2016) 181–186. https://doi.org/10.1007/s40090-016-0078-8.

[87] G.L. Schieber, E.B. Stechel, A. Ambrosini, J.E. Miller, P.G. Loutzenhiser, H2O splitting via a two-step solar thermoelectrolytic cycle based on non-stoichiometric ceria redox reactions: Thermodynamic analysis, Int. J. Hydrogen Energy. 42 (2017) 18785–18793. https://doi.org/10.1016/j.ijhydene.2017.06.098.

[88] E. Aneggi, C. de Leitenburg, M. Boaro, P. Fornasiero, A. Trovarelli, Catalytic applications of cerium dioxide, Elsevier Inc., 2020. https://doi.org/10.1016/b978-0-12-815661-2.00003-7.

[89] W.C. Chueh, C. Falter, M. Abbott, D. Scipio, P. Furler, S.M. Haile, S. Aldo, Solar-Driven Thermochemical Dissociation of CO 2 and H 2 O Using Ceria Using g the Sun to Make Fuels, Science (80-.). 330 (2010) 1797–1802.

[90] P. Furler, J. Scheffe, M. Gorbar, L. Moes, U. Vogt, A. Steinfeld, Solar thermochemical CO2 splitting utilizing a reticulated porous ceria redox system, Energy and Fuels. 26 (2012) 7051–7059. https://doi.org/10.1021/ef3013757.

[91] A. Trovarelli, Structural and oxygen storage/release properties of CeO2-based solid solutions, Comments Inorg. Chem. 20 (1999) 263–284. https://doi.org/10.1080/02603599908021446.

[92] T. Matsukawa, A. Hoshikawa, E. Niwa, M. Yashima, T. Ishigaki, Crystal structure of blue-colored ceria during redox reactions in a hydrogen atmosphere, CrystEngComm. 20 (2018) 155–158. https://doi.org/10.1039/c7ce02035j.

[93] M. Schaube, R. Merkle, J. Maier, Oxygen exchange kinetics on systematically doped ceria: A pulsed isotope exchange study, J. Mater. Chem. A. 7 (2019) 21854–21866. https://doi.org/10.1039/c9ta05908c.

[94] X. Zhang, K.J. Klabunde, Superoxide (O2) on the Surface of Heat-Treated Ceria. Intermediates in the Reversible Oxygen to Oxide Transformation, Inorg. Chem. 31 (1992) 1706–1709. https://doi.org/10.1021/ic00035a034.

[95] J.A. Lane, J.A. Kilner, Oxygen surface exchange on gadolinia doped ceria, Solid State Ionics. 136–137 (2000) 927–932. https://doi.org/10.1016/S0167-2738(00)00530-0.

[96] M. Bilke, P. Losch, O. Vozniuk, A. Bodach, F. Schüth, Methane to Chloromethane by Mechanochemical Activation: A Selective Radical Pathway, J. Am. Chem. Soc. 141 (2019) 11212–11218. https://doi.org/10.1021/jacs.9b04413.